Modeling the impacts of urbanization and open water surface on heavy convective rainfall: a case study over the emerging Xiong'an city, China

Article

Accepted Version

Modeling the Impacts of Urbanization and Open Water Surface on Heavy Convective Rainfall: A Case Study over the Emerging Xiong'an City, China

Yue Xing[1], Guangheng Ni[1], Long Yang[2, 3*], Yan Yang[1], Pei Xing[4] and Ting Sun[5]

[1]State Key Laboratory of Hydro-Science and Engineering, Department of Hydraulic Engineering, Tsinghua University, Beijing 100084, China

[2]School of Geography and Ocean Science, Nanjing University, Nanjing 210023, Jiangsu Province, China

[3]Department of Civil and Environmental Engineering, Princeton University, Princeton, NJ, USA

[4]Beijing Municipal Climate Center, Beijing 100089, China

[5]Department of Meteorology, University of Reading, Reading, RG6 6BB, UK

Corresponding author: Long Yang (yanglong86123@hotmail.com)

Key Points:

- Open water surface and urbanization show contrasting impact on heavy rainfall under strong large-scale forcing.
- Changes in rainfall accumulation highlight strong dependence of urban-induced rainfall anomalies on urbanization stages.
- Interactions between open water and urban surface contribute to downwind rainfall enhancement through intensified moist convection.

Abstract

In this study, we examine the impacts of urbanization and open water surface on heavy convective rainfall based on numerical modeling experiments using the Weather Research and Forecasting (WRF) model. We focus on a severe storm event over the emerging Xiong'an city in northern China. The storm event consists of two episodes, and features intense moisture transport and strong large-scale forcing. A set of WRF simulations were implemented to examine the sensitivity of spatiotemporal rainfall variability in and around the urban area to different land use scenarios. Modeling results highlight contrasting roles of open water and urban surface in dictating space-time organizations of convective rainfall under strong large-scale forcing. Dynamic perturbation to atmospheric forcing dominates the impacts of open water and urban surface on spatial rainfall distribution during the second storm episode, while urban surface promotes early initiation of convection during the first storm episode through enhanced buoyant energy. Open water surface contributes to convective inhibition through evaporative cooling but can enhance moist convection when the impact of urban surface is also considered. The synergistic effect of open water and urban surface leads to rainfall enhancement both over and in the downwind urban area. Changes in rainfall accumulation with different spatial extents of urban coverage highlight strong dependence of urban-induced rainfall anomalies on urbanization stages. Our results provide improved understandings on hydrometeorological impacts due to emerging cities in complex physiographic settings, and emphasize the importance of atmospheric forcing in urban rainfall modification studies.

1 Introduction

The impact of urbanization on rainfall has been extensively examined following the METROpolitan Meteorological Experiment (METROMEX, e.g., Changnon et al., 1971; Changnon et al., 1976) since the late 1970s. Modeling and observational studies show that urbanization has induced detectable rainfall anomalies both over and in the downwind urban areas (e.g., Ashley et al., 2012; Miao et al., 2009, 2011; Niyogi et al., 2011; Shepherd, 2005; Shepherd et al., 2002; Yang, et al., 2014a, 2014b; Yeung et al., 2015). There are three physical mechanisms associated with the phenomenon: (1) the "Urban Heat Island" effect increases surface temperature and promotes convection within the atmospheric boundary layer over urban areas (e.g., Bornstein & Lin, 2000; Collier, 2006; Dixon & Mote, 2003; Miao et al., 2009; Nie et al., 2017; Qiao et al., 2019; Souma et al., 2013); (2) increased surface roughness over urban canopy facilitates convergence (e.g., Loose & Bornstein, 1977; Shem & Shepherd, 2009); (3) urban aerosols influence rainfall microphysical processes through modifications on the physical and statistical properties of cloud condensation nuclei (e.g., Jin & Dickinson, 2010; Jin et al., 2005; Ntelekos et al., 2009).

Despite existing research results, our understanding of rainfall modification by urban environments is far from complete, especially for heavy convective rainfall under strong large-scale forcing (e.g., monsoon, extratropical system, tropical cyclone) (Paul et al., 2018; Reames & Stensrud, 2018; Singh et al., 2016; Zhang et al., 2018). For instance, Yang et al. (2014a) investigated the impact of urbanization on a severe thunderstorm under strong large-scale forcing over Milwaukee-Lake Michigan region. Their analyses show urbanization does not change cloud structure at regional scales but can modify space-time organizations of extreme rainfall around the city. Heavy convective rainfall under strong large-scale forcing is responsible for severe flooding over urban areas, which is a major concern in recent decades under the context of rapid

urbanization and booming urban population all over the world. McLeod et al. (2017) highlight the importance of considering flow regimes in urban rainfall modification studies based on climatological analyses of spatial-temporal rainfall patterns over Atlanta, Georgia. It is an important issue for storm cases with strong large-scale forcing since flow regimes determine key features of the pre-storm environment as well as advection of moisture that feeds the storm. In this study, we focus on heavy convective rainfall with contrasting flow regimes under strong large-scale forcing.

Urban impacts on rainfall for cities in complex physiographic settings (e.g., land-water boundaries, complex terrain) are still poorly understood due to the complexity of topography-related circulations and urban effects (e.g., Fernando, 2010; Freitag et al., 2018; Ganbat et al., 2015; Lin et al., 2011; Ryu et al., 2016; Shepherd et al., 2010). In this study, we focus on cities that are characterized by distinct land-water boundaries (i.e., lake). The impact of open water surface on rainfall and regional climate has been extensively examined in previous studies (e.g., Anyah et al., 2006; Chuang & Sousounis, 2003; Laird et al., 2009; Long et al., 2007; Notaro et al., 2013; Sousounis & Mann, 2000; Stivari et al., 2003; Sun et al., 2015; Wilson, 1977). The evaporative cooling effect of open water surface leads to a stable atmospheric boundary layer that inhibits convection and rainfall (e.g., Changnon, 1984; Farley Nicholls & Toumi, 2014). Gu et al. (2016) found that the impact of lake on local summer precipitation is negative during the day, and is positive during the night. The presence of urban areas by lakeside can enhance thermodynamic contrast between land and water that generate complex interactions between the lake-land breeze and urban-induced circulation. The evolution speed and penetration depth of lake-land breeze front can be greatly enhanced due to the presence of cities (e.g., Carter et al., 2012; Lin et al., 2008; Lo et al., 2007; Ohashi & Kida, 2002). For instance, Yang et al. (2014a) found that thermodynamic perturbation induced by urban surface enhances the intrusion of lake breeze and promotes the formation of a convergence zone over the northern boundary of Milwaukee (by the side of Lake Michigan) (similarly see, e.g., Shepherd & Burian, 2003; Shepherd et al., 2010 for studies over Houston). Unlike previous studies that focus on cities in the vicinity of an open water surface with a large spatial extent (i.e., typically lakes or oceans), we consider cities with a water body of its spatial extent less than or comparable to the size of the city itself. Theeuwes et al. (2013) modeled the influence of open water surfaces on summertime temperature and thermal comfort within a city. Open water surface contributes to both evaporative cooling for convective inhibition and additional moisture sources for moist convection, which demonstrates sharp contrast to the urban impact on convective rainfall. In this study, we shed light on the interrelated roles of contrasting thermodynamic and dynamic properties between open water and urban surface in dictating spatial and temporal variability of heavy convective rainfall.

Our study region is the emerging Xiong'an New Area (XNA, Figure 1), a new national-level district initiated by the Chinese government in 2017 to form the Beijing-Tianjin-Hebei (BTH) economic triangle for coordinated regional development. The initial urban coverage for XNA is 100 km^2 with a projected extent of 200 km^2 for its mid-term development. In the long run, Xiong'an city will be developed into a metropolis of 2000 km^2 (a comparable spatial extent of Beijing). It is noted the Baiyang Lake, an open water surface of 360 km^2 in XNA, may have potential impact on regional hydrometeorological processes. Improved understandings on the impact are thus critical for better regional planning of the BTH economic triangle.

The main objective of this study is to examine the impacts of open water and urbanization on heavy convective rainfall under strong large-scale forcing. Extreme rainfall over the study region is frequently associated with interactions of mid-latitude weather systems and moisture transport during the East Asian Summer Monsoon period. We focus on a severe storm event on 20 July 2016 over northern China. Our analyses are principally motivated by the following hypotheses: (1) contrasting impacts of open water and urban surface on spatiotemporal rainfall variability originate from thermodynamic and dynamic contrasts of surface properties as well as synoptic flow regimes; (2) cumulative rainfall over XNA and in the downwind region increases with the expanding spatial extent of urban coverage; (3) open water surface synergistically enhances moist convection with urban surface when the spatial extent of two surfaces are comparable. We examine these hypotheses based on high-resolution numerical simulations using a non-hydrostatic, fully comprehensible, mesoscale meteorological model, Weather Research and Forecasting (WRF) (Skamarock et al., 2008), with contrasting land use/land cover configurations.

The rest of the paper is organized as follows. In section 2, we describe observations, model configurations as well as details of the experiment setup. Results and discussions are provided in section 3, followed by section 4 for summary and conclusions.

2 Data and Methodology

2.1 Observations

We use three types of observations to evaluate the model performance:

a) Hourly observations of 2-m air temperature, 2-m relative humidity, 10-m wind speed, rain rate collected at 30 national weather stations (see Figure 1 for site locations) quality-controlled by CMA (Chinese Meteorological Administration) to examine the near-surface meteorology.

b) Hourly fusion precipitation product of automatic station and CMORPH (CPC MORPHing technique) at a spatial resolution of 0.1 degree to characterize the spatiotemporal rainfall variability (e.g., Chun-Hua et al., 2014).

c) Radiosonde observations of temperature, mixing ratio and wind speed (see Figure 1 for site location) to investigate the vertical profiles of synoptic conditions before and during the storm event.

2.2 Model configuration

The Advanced Research version WRF (ARW) version 3.7 is used in this study. The study area XNA is represented in three two-way nested domains (spatial extents of 200×200, 220×220 and 187×211 horizontal grids, with the corresponding resolution of 9 km, 3 km, and 1 km, respectively; Figure 1a). The outermost domain covers most of the central and northeastern China, while the innermost domain covers XNA and its surrounding region, including the southern part of Beijing and the western part of Tianjin (Figure 1b). The grids contain 54 sigma levels, with the upper boundary set at 50 hPa. The integral time step for the outer domain is 15 s. The initial and boundary conditions are provided by the National Center for Environmental Prediction (NCEP) Global Final Analysis (FNL) at a spatial and temporal resolution of 1 degree

and 6 hours, respectively. The 21-category MODIS dataset is used to represent land use and land cover in the study region.

Previous studies show that rainfall simulations are very sensitive to microphysics schemes adopted in atmospheric models, with planetary boundary layer scheme, radiation scheme, and other parameterizations playing a relatively smaller role (e.g., Efstathiou et al., 2013; Liu et al., 2011; Singh et al., 2018). We carried out sensitivity experiments over the study region for the 20 July 2016 storm (see section 3.1 for detailed descriptions of the case) with WRF simulations using different microphysics schemes, including WSM3, WSM5, and WSM6. The WRF simulation with WSM5 (Hong et al., 2004) shows the best performance against observations (not shown): we thus choose WSM5 as the microphysical parametrization in our following experiments. The other physics options configured in the model include: the MYJ planetary boundary layer (PBL) scheme (Janjić, 1994), the Dudhia shortwave radiation scheme (Dudhia, 1989), the Rapid Radiative Transfer Model (RRTM) longwave radiation scheme (Mlawer et al., 1997), Noah land surface model (Chen & Dudhia, 2001) and Monin-Obukhov Surface Layer scheme (Monin & Obukhov, 1954). Cumulus scheme is turned off for all domains due to the fine spatial resolution of horizontal grids (less than 10 km, e.g., Stensrud, 2009). In this study, we incorporate the multi-layer lake scheme by Subin et al. (2012) in WRF (Gu et al., 2015) to accurately depict the variations of heat, moisture, and momentum over the Baiyang Lake. In addition, the single-layer Urban Canopy Model (UCM) in WRF (see Chen et al., 2011 for details) is also used to accurately represent the thermal and dynamic properties of urban land surfaces with the default UCM parameters. Table 1 provides a summary of all key physics schemes used in WRF simulations of this study.

2.3 Experimental setup

To assess the urban-lake effects six WRF scenarios are set up (Table 2):

a) *control* scenario (CTRL, Figure 2a): Only the Baiyang Lake is considered with a small portion of urban coverage distributed to the southeast of the Lake, representing the present land use conditions over this region. This scenario is compared against in-situ observations to evaluate model performance (see section 3.2).

b) *urban* scenario (URB, Figure 2b): Baiyang Lake is set as in CTRL with its surrounding rural area replaced by urban surfaces, representing the maximum urbanization extent over XNA.

c) *baseline* scenario (BASE, Figure 2c): Baiyang Lake is removed from the CTRL scenario by replacing the water surface with cropland (i.e., the dominant land use type surrounding the city). Comparisons between CTRL/URB and BASE scenarios will be used to examine the impacts of open water and urban surface on rainfall.

d) Three other development scenarios of XNA (ULS, ULM, and ULL, Figure 2d, 2e and 2f, respectively): these additional urbanization scenarios (ULS, ULM, and ULL, with 120, 410, and 1417 urban grids, respectively; the total sizes are summarized in Table 2), are set up by replacing the outskirts of Baiyang Lake with cropland to mimic projected developments of XNA.

All the numerical experiments adopt the same model configurations as depicted in section 2.2 and summarized in Table 1, with land use/land cover being the only model difference. All the simulations are initiated at 00 UTC 17 July 2016 and run till 00 UTC 22 July 2016. The first 40 hours are regarded as model spin-up and are not included in the following analyses.

3 Results and Discussion

3.1 Synoptic background of 20 July 2016 storm

The 20 July 2016 storm persisted for more than 40 hours and produced widespread extreme rainfall over Beijing, Tianjin, and Hebei province. Nine state-level weather stations in Beijing recorded history-breaking rain rates (Gan et al., 2017). The maximum hourly rain rate is 56.8 mm h^{-1}. Maximum rainfall accumulation is 454 mm. The 20 July 2016 storm is associated with the evolution of a cold vortex and its interactions with the East Asian Summer Monsoon system. The pre-storm environment is characterized by strong moisture transport driven by the West Pacific Subtropical High that brings abundant warm and moist air plume to northern China. Meanwhile, the cold vortex gradually evolves from northwest to northern China, with cold air running down from the north (Figure 3). The low-pressure system promotes mesocyclogenesis and convection that leads to development of several mesoscale convective systems in northern China. Convective available potential energy (CAPE) is 872 J kg^{-1} at 00 UTC 19 July based on the radiosonde observation. Surface mixing ratio is around 18 g kg^{-1} at 12 UTC 19 UTC. The cold-air intrusion increases the baroclinicity of the atmosphere and serves as a strong catalyst for strong convection over the study region. The strengthening subtropical high and its extension to inland China "block" the track of the cold vortex, and ultimately provide a favorable environment for long-lasting convective outbreaks and extreme rainfall over northern China. Mesoscale topography (i.e., the Taihang Mountains to the northwest of domain 3) also plays a role in maintaining and enhancing convective intensity. There is a local maximum of wind speed over 20 m s^{-1} around the altitude of 1 km around 00 UTC 20 July (before the peak rain rates) , indicating that low-level jet as an additional ingredient for the 20 July 2016 storm.

The storm event consists of two storm episodes with changing synoptic flow regimes. The first storm episode (from 20 UTC 18 July to 14 UTC 19 July) is characterized with steering level wind blowing from the southwest. There is only moderate rainfall over XNA during the first storm episode. The second storm episode (from 15 UTC 19 July to 13 UTC 20 July) is dominated by southerly/southeasterly flow with relatively larger wind speeds (i.e., strong forcing), and produces intense rainfall over XNA. Contrasting synoptic flows determine the way how interactions of synoptic forcing and topography (i.e., the orientation is southwest towards northeast, see Figure 1b) influence spatiotemporal rainfall variability in the study region for the 20 July 2016 storm.

3.2 Model evaluation

The CTRL simulation captures variations of thermodynamic variables and wind fields during the entire period of the 20 July 2016 storm (Figure 4). The simulated 2-m temperature is in good agreement with observations before the rain starts, while it is underestimated after the rainfall peak with bias within a reasonable range (Figure 4a). The model generally captures the variation of relative humidity quite well, with slight underestimation (in terms of the median values) before and after rainfall (Figure 4b). The model reproduces key evolution features of surface wind fields during the entire simulation period, with slight overestimation after the peaking of rainfall (Figure 4c). Statistics, including Mean Bias, Root Mean Square Error (RMSE), correlation coefficient, and hit rate (HR) are calculated to quantitatively assess the model performance (Table 3): the hit rate for both 2-m temperature and rain rate exceeds 0.9; while correlation coefficient for 10-m wind speed is 0.78, indicating consistency between the

model simulation and in-situ observations. These statistics are comparable to previous studies (e.g., Zhang et al., 2017). Hourly rain rate peaks at around 22 UTC 19 July with a range from 10 mm h^{-1} to 30 mm h^{-1} (Figure 4d). The Mean Bias, RMSE and correlation between rain rate observation and simulation are 0.06, 4.67, and 0.58, respectively. Both the simulated peak timing and intensity of rainfall range agree well with the in-situ observations (Figure 4d). There is a strong rainband across Hebei province and extends to Tianjin at 22 UTC 19 July. The maximum hourly rain rate is approximately 40 mm h^{-1}. The rainband slowly propagates towards north and maintains peak rain rates till 02 UTC 20 July (Figure 5). The CTRL simulation captures the space-time organization of the rain band and evolution feature of slow propagation reasonably well, which are the key elements of extreme rainfall for the 20 July 2016 storm over the study region. The CTRL simulation captures the vertical profile of dynamic and thermodynamic variables before and during the storm (Figure 6). Even though there is a slight underestimation in terms of vertical wind profiles, both model and radiosonde observations show a "wind nose" around 1 km above the ground during the peak rainfall hour (00 UTC 20 July), with the wind speed exceeding 20 m s^{-1}.

In general, the CTRL simulation captures the spatiotemporal rainfall variability, key features of thermodynamic variables and wind fields for the 20 July 2016 storm reasonably well. Critical elements for extreme rainfall are also well represented in the simulation (e.g., low-level jet).

3.3 Impact on rainfall: open water versus urban surface

Different temporal evolutions of rain rate averaged over the entire XNA (see the black dashed box in Figure 1) are produced by the CTRL, BASE and URB simulations (Figure 7a). Compared to the CTRL simulation, the BASE simulation shows an earlier initiation of the second storm episode and produces less total rainfall over XNA region by 4 mm and 2 mm for the first and second storm episodes, respectively, indicating a positive influence of the open water surface on rainfall. The urban impact on rainfall is different from that of the lake. We notice an enhanced rainfall peak during the first storm episode in the URB simulation which contributes to increased total rainfall (~32 mm), compared to the BASE simulation (Figure 7c). Three distinct "spikes" of hourly rain rates are noted during the second storm episode in the URB simulation, as opposed to the single dominant rainfall peak in either BASE or CTRL simulation (Figure 7a). However, the total rainfall over XNA is decreased by 12 mm in the URB simulation during the second storm episode compared to the BASE simulation (Figure 7c).

The spatial distribution of rainfall differences between CTRL, URB and BASE simulations is remarkable for the two storm episodes (Figure 8). Consistent with temporal evolution difference (cf. Figure 7a), the presence of the city increases rainfall over XNA during the first storm episode (Figure 8b). In addition to rainfall differences over XNA, strong rainfall enhancement is also observed over the upwind region for both the CTRL and URB simulation during the second storm episode, while only weak rainfall anomalies are scattered in either the upwind or downwind region for the first storm episode (Figure 8). Rainfall contrasts between the first and second storm episode highlight the importance of flow regimes in dictating hydrometeorological impacts due to land use/land cover changes. The opposite sign of rainfall changes during the second storm episode between CTRL and URB (Figure 7c) is associated with the thermodynamic contrasts of open water and urban surfaces, as will be further elaborated below.

Open water surface contributes to the increase in near-surface specific humidity (~1 g kg^{-1}) and decrease in air temperature (~0.5 K) through enhanced evaporation during the first storm episode (Figure 9a). As contrary in the URB simulation, we see a pronounced increase of near-surface temperature (~1.5 K) over the entire urban coverage but mixed changes (i.e., both increase and decrease) in 2-m specific humidity (Figure 9b). Strong surface warming provides additional buoyant energy for convection over XNA that leads to earlier initiation of rainfall in the URB simulation (Figure 7a). Slight rainfall increase in the CTRL simulation is tied to elevated near-surface moisture over the lake, with the timing of rainfall kept the same as the BASE simulation (Figure 7a). Due to the large heat capacity of the water body, there is a slight increase in surface temperature (~0.8 K) and specific humidity (~0.5 g kg^{-1}) in the CTRL simulation compared to the BASE simulation after the first storm episode (Figure 9c). However, the city-induced surface warming effect is alleviated after the first storm episode in the URB simulation, with negligible temperature differences observed over XNA (Figure 9d).

In addition to the thermodynamic perturbations induced by open water and urban surface, noticeable perturbations exist in the near-surface wind fields due to increased (decreased) surface roughness in the URB (CTRL) simulation (Figure 9e-9h). Changes in the 10-m wind fields are consistent for both storm episodes with more significant changes for the second one. Increased surface roughness in the URB simulation reduces surface wind speed during the second storm episode, and creates an upwind convergence zone of XNA for increased rainfall (Figure 8d). Decreased rainfall over XNA during the second storm episode in the URB simulation is contributed by the depletion of atmospheric moisture content during the first storm episode and reduced moisture advection during the second storm episode.

We further examine the vertical wind profiles along the dominant wind vectors (Line AB and Line CD in Figure 8) for the two storm episodes (Figure 10), providing direct evidence that is responsible for the rainfall anomalies. For the first storm episode, the entire atmospheric column is characterized with a strong updraft over the urban area in the URB simulation, while for the CTRL simulation, updraft only exists in the lower atmosphere (below 1 km) underneath the downdraft over the lake. Without the lake or urban area (i.e., BASE simulation), there are stable horizontal wind vectors in the lower atmosphere with only a small updraft intensity before the rain. For the second storm episode, both the CTRL and URB simulations show enhanced updraft in the upwind boundary of the lake and urban area.

We provide moisture budget analysis for the storm event of all three simulations, i.e., CTRL, URB, and BASE, in Figure 11a, 11b, and 11c. The overall contribution of evaporation is relatively small to total rainfall. In addition, evaporation is much smaller in the URB simulation than the other two simulations. Rainfall rates are consistently changed with convergence, indicating the role of moisture transport in determining rainfall intensity over XNA. Rainfall anomalies for the first storm episode are mainly due to thermodynamic perturbations induced by the presence of open water and urban surface. The thermodynamic contrast fades out after the first storm episode, and thus contributes marginally to rainfall changes over XNA region during the second storm episode. It is the strong atmospheric forcing with advection of unstable air plume that dominates the heavy rainfall process during the second storm episode. The increased (decreased) rainfall over the upwind (downwind) of XNA is mainly due to dynamic perturbations on atmospheric forcing that leads to bifurcation upwind of XNA. Rainfall anomalies (especially over XNA) induced by urban surface and the lake highlights contrasting roles of urban and water surface in modulating extreme rainfall events. We further investigate

the impacts of different spatial extents of urban coverages on spatiotemporal rainfall variability for the 20 July 2016 storm, with the influence of open water surface included.

3.4 Impact of urbanization on rainfall

Compared to the CTRL simulation, three urbanization simulations (i.e., ULS, ULM, and ULL) initiate earlier rainfall during the first storm episode (Figure 7b). Rainfall accumulation for both the first and second storm episode increases with the spatial extent of urban coverage over XNA, highlighting the strong dependence of urban-induced rainfall anomalies on urbanization stages (similarly see Miao et al., 2011). Comparisons between the three urbanization simulations and the CTRL simulation highlight the role of the open water surface in producing rainfall anomalies over XNA region associated with the expanding urban coverages. For instance, rainfall accumulation for the second storm episode in the ULL simulation (representing a full urbanization stage) is larger than the CTRL simulation by 10 mm. Given the role of urban surface in decreasing rainfall over XNA shown in the URB simulation (without the lake), we highlight that the presence of Baiyang lake increases rainfall over XNA through synergistic effects between open water and urban surface (Figure 7c).

We further show spatial distribution of rainfall differences for the two storm episodes between the three urbanization simulations and the CTRL simulation in Figure 12. In addition to rainfall changes over XNA, we find consistent rainfall increases in the downwind of XNA for both storm episodes. A monotonic rainfall enhancement is observed with urban coverage across the three urbanization simulations (Figure 12). The maximum rainfall increase appears ~100 km (~80 km) downwind of XNA for the first (second) storm episode; whereas such downwind rainfall enhancement is observed in neither CTRL nor URB (cf. Figure 8). Similar to the URB simulation, we see bifurcated low-level wind fields in the upwind of XNA, which contributes to decreased rainfall accumulation during the second storm episode for the ULS and ULM simulations. However, there is increased rainfall accumulation for the second storm episode in the ULL simulation compared to either CTRL or BASE (Figure 7c). We further show rainfall difference between the ULL and URB simulations in Figure 12. The only difference between the ULL and URB simulation is that the "lake-shaped" urban land surface in the URB simulation is replaced by open water surface (Figure 2 and Table 2). We find similar features of downwind rainfall enhancement, with relatively larger rainfall difference for both storm episodes in ULL than URB (Figure 12d and 12h), indicating the positive role of synergistic effects between open water and urban surface in determining rainfall anomalies over both XNA and its downwind region. A possible explanation is that the surface warming effect contributed by the urban surface facilitates moist convection together with the additional moisture availability contributed by open water surface (as elaborated in Section 3.3). The moist, unstable air plume advects downwind XNA region and leads to increased convective activity. Increased moisture advection is further confirmed in the moisture budget analysis: the peak convergence is 36.8 mm h^{-1} for ULL, while it is 22.8 mm h^{-1} and 24.5 mm h^{-1} for URB and CTRL, respectively (Figure 11d-f).

Figure 13 shows the differences in the spatial distribution of the thermodynamic and dynamic variables between the three urbanization simulations and the CTRL simulations. Expanding urban coverages contribute to increase near-surface air temperature over and surrounding the urban area: the average 2-m air temperature over urban areas is increased by 0.8 K, 1.6 K, and 2 K in ULS, ULM and ULL, respectively. The temperature anomalies can extend up to 1.5 km above the ground in the three urbanization simulations (figures not shown),

indicating the urbanization-induced warming potential on the lower atmosphere. Changes in 2-m specific humidity vary with the expanding urban coverages. For instance, the ULM simulation presents the maximum increase in 2-m specific humidity by up to 1.6 g kg^{-1} over XNA, while only slight differences are produced by ULS and ULL (Figure 13a-13c). Changes of near-surface specific humidity are tied to moisture variations in the lower atmosphere. Like the URB simulation, we observe consistent decreases in 10-m wind speed with expanding urban coverages in the three urbanization simulations (Figure 13g-i).

Differences in thermodynamic and dynamic variables can lead to contrasting potentials for convection as indicated by Lifted index (LI, Figure 14). LI is the temperature difference between the environmental temperature at 500 hPa and the temperature of an air parcel lifted adiabatically from the surface to 500 hPa. LI is negative throughout the rainfall process, indicating that the atmosphere is unstable. Before the start of the first storm episode, LI is less than -5, indicating that the atmosphere is very unstable. LI can reach -7 to -8 near the city, indicating the impact of urban surface in promoting convection. The instability of the atmosphere is relatively weak in the scenario without city (Figure 14a and 14c) or with a smaller urban coverage (Figure 14d). After the first storm episode, the atmospheric instability is reduced (with LI around -3). The instability is comparatively higher for the scenarios with presence of urban or lake than the BASE simulation (Figure 14g, 14h, and 14j-14l).

We further characterize the pre-storm environment of both the first and second storm episode based on convective available potential energy and convective inhibition (CIN). Cross sections of CAPE along line AB (Figure 15) show increased values over the urban area. The region with CAPE exceeding 900 J kg^{-1} is confined within the lake zone, while it extends to downwind of XNA region for the three urbanization simulations. The CIN is decreased by 10 J kg^{-1} over the urban area. In addition, the positive CAPE penetrates to 4 km above the ground over urban areas for ULM and ULL, while for both CTRL and ULS, the atmospheric boundary layer is capped by an inversion layer at ~2 km above the ground. Large CAPE indicates strong vertical velocities for convection, as can be seen from the vertical profiles of vertical velocity (Figure 16). Both ULM and ULL simulations show strong updraft over XNA, while for the ULL simulation, the updraft extends downwind of XNA. We can also see that strong convection enhances atmospheric moisture content (Figure 16, contour) in ULM and ULL. At the beginning of the second storm episode, CAPE in the ULS, ULM and ULL simulation is ~100 J kg^{-1} larger than that in CTRL (Figure 15). Unlike the vertical wind profiles during the first storm episode, locations of updraft vary along the cross section during the second storm episode, even though we observe slightly larger vertical velocities in ULM and ULL (Figure 16f and 16h). Consistent updrafts are observed at 180 km along the cross section across the three urbanization and CTRL simulations, which are probably due to the forced lifting of regional topography to the northwest of XNA region (i.e., Taihang Mountains). Interactions between synoptic forcing and topography play an important role in rainfall enhancement over the downwind of XNA. The synoptic flow (southwesterly) aligns with the topography that minimizes its impact on rainfall anomalies during the first storm episode. Our results show rainfall anomalies induced by expanding urban coverages over XNA can extend to regional scales, and warrants particular attention for metropolis (e.g., Beijing) downwind from XNA.

4 Summary and Conclusions

In this study, we examined the 20 July 2016 storm that produced widespread flooding and extreme rainfall over northern China. Sensitivity simulations based on the WRF model (coupled with a lake Model and a single-layer urban canopy model) with contrasting land-use scenarios were implemented to investigate the impacts of open water surface (i.e., lake) and urbanization on spatiotemporal rainfall variability over the emerging Xiong'an (XNA) city in northern China. The main findings are summarized below.

(1) The 20 July 2016 storm is mainly attributed to interactions of a slowly-evolving cold vortex and moisture transport during the East Asian Summer Monsoon period. The storm event consists of two storm episodes with contrasting flow regimes, and is characterized with strong large-scale forcing (e.g., baroclinicity, LLJ). The CTRL simulation captures key elements of the 20 July 2016 storm, including temporal variations of dynamic and thermodynamic fields during the entire storm period. The simulated spatiotemporal rainfall variability agrees well with CMORPH rainfall product and gauge observations.

(2) Model sensitivity experiments with different land surface configurations highlight contrasting roles of open water and urban surface in determining spatial and temporal organization of extreme rainfall. Urban surface provides additional buoyant energy that allows convection to occur earlier in the URB simulation than the CTRL simulation (with only the presence of the lake) during the first storm episode, while the open water surface contributes atmospheric moisture availability and increased rainfall over XNA. Dynamic perturbation (i.e., changes in surface roughness) to atmospheric forcing dominates rainfall anomalies during the second storm episode for both URB and CTRL simulations. Rainfall contrasts between the two storm episodes highlight the importance of flow-regime analyses in understanding hydrometeorological impact due to land use/land cover changes.

(3) Changes in rainfall accumulation over XNA under different urbanization scenarios highlight strong dependence of urban-induced rainfall anomalies on the spatial extent of urban surfaces. The observed rainfall enhancement in the downwind of XNA for both storm episodes indicates that impacts of urbanization on rainfall are not confined within the proximity of urban areas, but can be transferred to regional scales.

(4) Comparisons between the URB (with the presence of only urban land surface) and ULL (with the presence of both urban and lake) simulations highlight the synergistic impacts of open water and urban surface on spatial rainfall distribution. The synergistic impact can be identified when the spatial extents of water surface and urban surface are comparable. The enhanced moist, unstable air plume contributed by evaporation from the open water and urban surface can be advected downwind of XNA region, and leads to intensified convection and rainfall.

Our modeling results highlight interrelated roles of contrasting land surface properties in dictating spatial and temporal variability of extreme rainfall, and contribute to improved understandings on hydrometeorological processes over complex physiographic settings. The emerging XNA in northern China is the showcase of dramatic anthropogenic modification on land use/land cover and provides opportunities to investigate its consequences on regional climate and extreme weather events associated with those changes. Numerical model experiments provide useful tools to look into the physical processes and guide city designs and regional planning. One limitation to appreciate is that a single storm event is analyzed in the

present study, and thus warrants caution of any generalization from the results. Future studies should include analyses of additional storm events with diverse synoptic conditions.

Acknowledgments

YX, GN, and YY acknowledge the support from National Natural Science Foundation of China (51679119) and The National Key Research and Development Program of China (2018YFA0606002). TS acknowledges the support from NERC Independent Research Fellowship (NE/P018637/1). The WRF simulations were implemented on Tianhe-2 National Supercomputer Center in Guangzhou, China. Surface observational dataset is accessible from http://www.urbanhydromet.org/en/. The radiosonde observation is maintained by the University of Wyoming (http://weather.uwyo.edu/upperair/sounding.html). Precipitation fusion product of automatic station and CMORPH can be obtained from National Meteorological Information Center (http://data.cma.cn/en).

References

Anyah, R. O., Semazzi, F. H., & Xie, L. (2006). Simulated physical mechanisms associated with climate variability over Lake Victoria basin in East Africa. Monthly Weather Review, 134(12), 3588-3609. https://doi.org/10.1175/MWR3266.1

Ashley, W. S., Bentley, M. L., & Stallins, J. A. (2012). Urban-induced thunderstorm modification in the Southeast United States. Climatic Change, 113(2), 481-498. https://doi.org/10.1007/s10584-011-0324-1

Bornstein, R., & Lin, Q. (2000). Urban heat islands and summertime convective thunderstorms in Atlanta: Three case studies. Atmospheric Environment, 34(3), 507-516. https://doi.org/10.1016/S1352-2310(99)00374-X

Carter, M., Shepherd, J. M., Burian, S., & Jeyachandran, I. (2012). Integration of lidar data into a coupled mesoscale–land surface model: a theoretical assessment of sensitivity of urban–coastal mesoscale circulations to urban canopy parameters. Journal of Atmospheric and Oceanic Technology, 29(3), 328-346. https://doi.org/10.1175/2011JTECHA1524.1

Changnon Jr, S. A. (1984). Urban and lake effects on summer rainfall in the Chicago area. Physical Geography, 5(1), 1-23. https://doi.org/10.1080/02723646.1984.10642240

Changnon Jr, S. A., Huff, F. A., & Semonin, R. G. (1971). METROMEX: an investigation of inadvertent weather modification. Bulletin of the American Meteorological Society, 52(10), 958-968. https://doi.org/10.1175/1520-0477(1971)052<0958:MAIOIW>2.0.CO;2

Changnon Jr, S. A., Semonin, R. G., & Huff, F. (1976). A hypothesis for urban rainfall anomalies. Journal of Applied Meteorology, 15(6), 544-560. https://doi.org/10.1175/1520-0450(1976)015<0544:AHFURA>2.0.CO;2

Chen, F., & Dudhia, J. (2001). Coupling an advanced land surface–hydrology model with the Penn State–NCAR MM5 modeling system. Part I: Model implementation and sensitivity. Monthly Weather Review, 129(4), 569-585. https://doi.org/10.1175/1520-0493(2001)129<0569:CAALSH>2.0.CO;2

Chen, F., Kusaka, H., Bornstein, R., Ching, J., Grimmond, C., Grossman-Clarke, S., et al. (2011). The integrated WRF/urban modelling system: development, evaluation, and

applications to urban environmental problems. International Journal of Climatology, 31(2), 273-288. https://doi.org/10.1002/joc.2158

Chuang, H.-Y., & Sousounis, P. J. (2003). The impact of the prevailing synoptic situation on the lake-aggregate effect. Monthly Weather Review, 131(5), 990-1010. https://doi.org/10.1175/1520-0493(2003)131<0990:TIOTPS>2.0.CO;2

Chun-Hua, S., Dong, G., Hui, L., Bin, Z., & Ren-Qiang, L. (2014). Stratosphere-troposphere Exchange corresponding to a deep convection in the warm sector and abnormal subtropical front induced by a cutoff low over East Asia. Chinese Journal of Geophysics, 57(1), 1-10. https://doi.org/10.1002/cjg2.20079

Collier, C. G. (2006). The impact of urban areas on weather. Quarterly Journal of the Royal Meteorological Society, 132(614), 1-25. https://doi.org/10.1256/qj.05.199

Dixon, P. G., & Mote, T. L. (2003). Patterns and causes of Atlanta's urban heat island–initiated precipitation. Journal of Applied Meteorology, 42(9), 1273-1284. https://doi.org/10.1175/1520-0450(2003)042<1273:PACOAU>2.0.CO;2

Dudhia, J. (1989). Numerical study of convection observed during the winter monsoon experiment using a mesoscale two-dimensional model. Journal of the Atmospheric Sciences, 46(20), 3077-3107. https://doi.org/10.1175/1520-0469(1989)046<3077:NSOCOD>2.0.CO;2

Efstathiou, G., Zoumakis, N., Melas, D., Lolis, C., & Kassomenos, P. (2013). Sensitivity of WRF to boundary layer parameterizations in simulating a heavy rainfall event using different microphysical schemes. Effect on large-scale processes. Atmospheric Research, 132, 125-143. https://doi.org/10.1016/j.atmosres.2013.05.004

Farley Nicholls, J., & Toumi, R. (2014). On the lake effects of the Caspian Sea. Quarterly Journal of the Royal Meteorological Society, 140(681), 1399-1408. https://doi.org/10.1002/qj.2222

Fernando, H. (2010). Fluid dynamics of urban atmospheres in complex terrain. Annual review of fluid mechanics, 42, 365-389. https://doi.org/10.1146/annurev-fluid-121108-145459

Freitag, B., Nair, U., & Niyogi, D. (2018). Urban modification of convection and rainfall in complex terrain. Geophysical Research Letters, 45(5), 2507-2515. https://doi.org/10.1002/2017GL076834

Gan, L., Guo, W., Deng, C., & Bureau, B. M. (2017). Comparative snalysis of two torrential rain processes in Beijing. Journal of Arid Meteorology. (in Chinese)

Ganbat, G., Seo, J. M., Han, J.-Y., & Baik, J.-J. (2015). A theoretical study of the interactions of urban breeze circulation with mountain slope winds. Theoretical and applied climatology, 121(3-4), 545-555. https://doi.org/10.1007/s00704-014-1252-6

Gu, H., Jin, J., Wu, Y., Ek, M. B., & Subin, Z. M. (2015). Calibration and validation of lake surface temperature simulations with the coupled WRF-lake model. Climatic Change, 129(3-4), 471-483. https://doi.org/10.1007/s10584-013-0978-y

Gu, H., Ma, Z., & Li, M. (2016). Effect of a large and very shallow lake on local summer precipitation over the Lake Taihu basin in China. Journal of Geophysical Research: Atmospheres, 121(15), 8832-8848. https://doi.org/10.1002/2015JD024098

Hong, S.-Y., Dudhia, J., & Chen, S.-H. J. M. W. R. (2004). A revised approach to ice microphysical processes for the bulk parameterization of clouds and precipitation. 132(1), 103-120. https://doi.org/10.1175/1520-0493(2004)132<0103:ARATIM>2.0.CO;2

Janjić, Z. I. (1994). The step-mountain eta coordinate model: Further developments of the convection, viscous sublayer, and turbulence closure schemes. Monthly Weather Review, 122(5), 927-945. https://doi.org/10.1175/1520-493(1994)122<0927:TSMECM>2.0.CO;2

Jin, M., & Dickinson, R. E. (2010). Land surface skin temperature climatology: benefitting from the strengths of satellite observations. Environmental Research Letters, 5(4), 044004. https://doi.org/10.1088/1748-9326/5/4/044004

Jin, M., Shepherd, J. M., & King, M. D. (2005). Urban aerosols and their variations with clouds and rainfall: a case study for New York and Houston. Journal of Geophysical Research: Atmospheres, 110(D10). https://doi.org/10.1029/2004JD005081

Laird, N., Sobash, R., & Hodas, N. (2009). The frequency and characteristics of lake-effect precipitation events associated with the New York State Finger Lakes. Journal of Applied Meteorology and Climatology, 48(4), 873-886. https://doi.org/10.1175/2008JAMC2054.1

Lin, C.-Y., Chen, F., Huang, J., Chen, W.-C., Liou, Y.-A., Chen, W.-N., & Liu, S.-C. (2008). Urban heat island effect and its impact on boundary layer development and land–sea circulation over northern Taiwan. Atmospheric Environment, 42(22), 5635-5649. https://doi.org/10.1016/j.atmosenv.2008.03.015

Lin, C.-Y., Chen, W.-C., Chang, P.-L., Sheng, Y.-F. (2011). Impact of the urban heat island effect on precipitation over a complex geographic environment in northern Taiwan. Journal of Applied Meteorology, 50(2), 339-353. https://doi.org/10.1175/2010JAMC2504.1

Liu, C., Ikeda, K., Thompson, G., Rasmussen, R., & Dudhia, J. (2011). High-resolution simulations of wintertime precipitation in the Colorado Headwaters region: Sensitivity to physics parameterizations. Monthly Weather Review, 139(11), 3533-3553. https://doi.org/10.1175/MWR-D-11-00009.1

Lo, J. C., Lau, A. K., Chen, F., Fung, J. C., & Leung, K. K. (2007). Urban modification in a mesoscale model and the effects on the local circulation in the Pearl River Delta region. Journal of Applied Meteorology and Climatology, 46(4), 457-476. https://doi.org/10.1175/JAM2477.1

Long, Z., Perrie, W., Gyakum, J., Caya, D., & Laprise, R. (2007). Northern lake impacts on local seasonal climate. Journal of Hydrometeorology, 8(4), 881-896. https://doi.org/10.1175/JHM591.1

Loose, T., & Bornstein, R. D. (1977). Observations of mesoscale effects on frontal movement through an urban area. Monthly Weather Review, 105(5), 563-571. https://doi.org/10.1175/1520-0493(1977)105<0563:OOMEOF>2.0.CO;2

McLeod, J., Shepherd, M., & Konrad II, C. E. (2017). Spatio-temporal rainfall patterns around Atlanta, Georgia and possible relationships to urban land cover. Urban Climate, 21, 27-42. https://doi.org/10.1016/j.uclim.2017.03.004

Miao, S., Chen, F., LeMone, M. A., Tewari, M., Li, Q., & Wang, Y. (2009). An observational and modeling study of characteristics of urban heat island and boundary layer structures in Beijing. Journal of Applied Meteorology and Climatology, 48(3), 484-501. https://doi.org/10.1175/2008JAMC1909.1

Miao, S., Chen, F., Li, Q., & Fan, S. (2011). Impacts of urban processes and urbanization on summer precipitation: A case study of heavy rainfall in Beijing on 1 August 2006. Journal of Applied Meteorology and Climatology, 50(4), 806-825. https://doi.org/10.1175/2010JAMC2513.1

Mlawer, E. J., Taubman, S. J., Brown, P. D., Iacono, M. J., & Clough, S. A. (1997). Radiative transfer for inhomogeneous atmospheres: RRTM, a validated correlated-k model for the longwave. Journal of Geophysical Research: Atmospheres, 102(D14), 16663-16682. https://doi.org/10.1029/97JD00237

Monin, A. S., & Obukhov, A. M. (1954). Basic laws of turbulent mixing in the surface layer of the atmosphere. Contrib. Geophys. Inst. Acad. Sci. USSR, 151(163), e187.

Nie, W., Zaitchik, B. F., Ni, G., & Sun, T. (2017). Impacts of anthropogenic heat on summertime rainfall in Beijing. Journal of Hydrometeorology, 18(3), 693-712. https://doi.org/10.1175/JHM-D-16-0173.1

Niyogi, D., Pyle, P., Lei, M., Arya, S. P., Kishtawal, C. M., Shepherd, M., et al. (2011). Urban modification of thunderstorms: An observational storm climatology and model case study for the Indianapolis urban region. Journal of Applied Meteorology and Climatology, 50(5), 1129-1144. https://doi.org/10.1175/2010JAMC1836.1

Notaro, M., Holman, K., Zarrin, A., Fluck, E., Vavrus, S., & Bennington, V. (2013). Influence of the Laurentian Great Lakes on regional climate. Journal of Climate, 26(3), 789-804. https://doi.org/10.1175/JCLI-D-12-00140.1

Ntelekos, A. A., Smith, J. A., Donner, L., Fast, J. D., Gustafson Jr, W. I., Chapman, E. G., & Krajewski, W. F. (2009). The effects of aerosols on intense convective precipitation in the northeastern United States. Quarterly Journal of the Royal Meteorological Society: A journal of the atmospheric sciences, applied meteorology and physical oceanography, 135(643), 1367-1391. https://doi.org/10.1002/qj.476

Ohashi, Y., & Kida, H. (2002). Local circulations developed in the vicinity of both coastal and inland urban areas: A numerical study with a mesoscale atmospheric model. Journal of Applied Meteorology, 41(1), 30-45. https://doi.org/10.1175/1520-0450(2002)041<0030:LCDITV>2.0.CO;2

Paul, S., Ghosh, S., Mathew, M., Devanand, A., Karmakar, S., & Niyogi, D. (2018). Increased spatial variability and intensification of extreme monsoon rainfall due to Urbanization. Scientific reports, 8(1), 3918. https://doi.org/10.1038/s41598-018-22322-9

Qiao, Z., Wu, C., Zhao, D., Xu, X., Yang, J., Feng, L., et al. (2019). Determining the Boundary and Probability of Surface Urban Heat Island Footprint Based on a Logistic Model. Remote Sensing, 11(11), 1368. https://doi.org/10.3390/rs11111368

Reames, L. J., & Stensrud, D. J. (2018). Influence of a Great Plains urban environment on a simulated supercell. Monthly Weather Review, 146(5), 1437-1462. https://doi.org/10.1175/MWR-D-17-0284.1

Ryu, Y.-H., Smith, J. A., Bou-Zeid, E., & Baeck, M. L. (2016). The influence of land surface heterogeneities on heavy convective rainfall in the Baltimore–Washington metropolitan area. Monthly Weather Review, 144(2), 553-573. https://doi.org/10.1175/MWR-D-15-0192.1

Shem, W., & Shepherd, M. (2009). On the impact of urbanization on summertime thunderstorms in Atlanta: Two numerical model case studies. Atmospheric Research, 92(2), 172-189. https://doi.org/10.1016/j.atmosres.2008.09.013

Shepherd, J. M. (2005). A review of current investigations of urban-induced rainfall and recommendations for the future. Earth Interactions, 9(12), 1-27. https://doi.org/10.1175/EI156.1

Shepherd, J. M., & Burian, S. J. (2003). Detection of urban-induced rainfall anomalies in a major coastal city. Earth Interactions, 7(4), 1-17. https://doi.org/10.1175/1087-3562(2003)007<0001:DOUIRA>2.0.CO;2

Shepherd, J. M., Carter, M., Manyin, M., Messen, D., & Burian, S. (2010). The impact of urbanization on current and future coastal precipitation: a case study for Houston. Environment and Planning B: Planning and Design, 37(2), 284-304. https://doi.org/10.1068/b34102t

Shepherd, J. M., Pierce, H., & Negri, A. J. (2002). Rainfall modification by major urban areas: Observations from spaceborne rain radar on the TRMM satellite. Journal of Applied Meteorology, 41(7), 689-701. https://doi.org/10.1175/1520-0450(2002)041<0689:RMBMUA>2.0.CO;2

Singh, J., Vittal, H., Karmakar, S., Ghosh, S., & Niyogi, D. (2016). Urbanization causes nonstationarity in Indian summer monsoon rainfall extremes. Geophysical Research Letters, 43(21). https://doi.org/10.1002/2016GL071238

Singh, K., Bonthu, S., Purvaja, R., Robin, R., Kannan, B., & Ramesh, R. (2018). Prediction of heavy rainfall over Chennai Metropolitan City, Tamil Nadu, India: impact of microphysical parameterization schemes. Atmospheric Research, 202, 219-234. https://doi.org/10.1016/j.atmosres.2017.11.028

Skamarock, W., Klemp, J., Dudhia, J., Gill, D., Barker, D., Duda, M., et al. (2008). A description of the advanced research WRF Version 3, NCAR technical note, Mesoscale and Microscale Meteorology Division. National Center for Atmospheric Research, Boulder, Colorado, USA.

Souma, K., Tanaka, K., Suetsugi, T., Sunada, K., Tsuboki, K., Shinoda, T., et al. (2013). A comparison between the effects of artificial land cover and anthropogenic heat on a localized heavy rain event in 2008 in Zoshigaya, Tokyo, Japan. Journal of Geophysical Research: Atmospheres, 118(20), 11,600-611,610. https://doi.org/10.1002/jgrd.50850

Sousounis, P. J., & Mann, G. E. (2000). Lake-aggregate mesoscale disturbances. Part V: Impacts on lake-effect precipitation. Monthly Weather Review, 128(3), 728-745. https://doi.org/10.1175/1520-0493(2000)128<0728:LAMDPV>2.0.CO;2

Stensrud, D. J. (2009). Parameterization schemes: keys to understanding numerical weather prediction models: Cambridge University Press, Cambridge.

Stivari, S. M., de Oliveira, A. P., Karam, H. A., & Soares, J. (2003). Patterns of local circulation in the Itaipu Lake area: numerical simulations of lake breeze. Journal of Applied Meteorology, 42(1), 37-50. https://doi.org/10.1175/1520-0450(2003)042<0037:POLCIT>2.0.CO;2

Subin, Z. M., Riley, W. J., & Mironov, D. (2012). An improved lake model for climate simulations: model structure, evaluation, and sensitivity analyses in CESM1. Journal of Advances in Modeling Earth Systems, 4(1). https://doi.org/10.1029/2011MS000072

Sun, X., Xie, L., Semazzi, F., & Liu, B. (2015). Effect of lake surface temperature on the spatial distribution and intensity of the precipitation over the Lake Victoria basin. Monthly Weather Review, 143(4), 1179-1192. https://doi.org/10.1175/MWR-D-14-00049.1

Theeuwes, N., Solcerová, A., & Steeneveld, G. (2013). Modeling the influence of open water surfaces on the summertime temperature and thermal comfort in the city. Journal of Geophysical Research: Atmospheres, 118(16), 8881-8896. https://doi.org/10.1002/jgrd.50704

Wilson, J. W. (1977). Effect of Lake Ontario on precipitation. Monthly Weather Review, 105(2), 207-214. https://doi.org/10.1175/1520-0493(1977)105<0207:EOLOOP>2.0.CO;2

Yang, L., Smith, J. A., Baeck, M. L., Bou-Zeid, E., Jessup, S. M., Tian, F., & Hu, H. (2014a). Impact of urbanization on heavy convective precipitation under strong large-scale forcing: A case study over the Milwaukee–Lake Michigan region. Journal of Hydrometeorology, 15(1), 261-278. https://doi.org/10.1175/JHM-D-13-020.1

Yang, L., Tian, F., Smith, J. A., & Hu, H. (2014b). Urban signatures in the spatial clustering of summer heavy rainfall events over the Beijing metropolitan region. Journal of Geophysical Research: Atmospheres, 119(3), 1203-1217. https://doi.org/10.1002/2013JD020762

Yeung, J. K., Smith, J. A., Baeck, M. L., & Villarini, G. (2015). Lagrangian analyses of rainfall structure and evolution for organized thunderstorm systems in the urban corridor of the northeastern United States. Journal of Hydrometeorology, 16(4), 1575-1595. https://doi.org/10.1175/JHM-D-14-0095.1

Zhang, W., Villarini, G., Vecchi, G. A., & Smith, J. A. (2018). Urbanization exacerbated the rainfall and flooding caused by hurricane Harvey in Houston. Nature, 563(7731), 384. https://doi.org/10.1038/s41586-018-0676-z

Zhang, Y., Miao, S., Dai, Y., & Bornstein, R. (2017). Numerical simulation of urban land surface effects on summer convective rainfall under different UHI intensity in Beijing. Journal of Geophysical Research: Atmospheres, 122(15), 7851-7868. https://doi.org/10.1002/2017JD026614

List of Tables

Table 1. Overview of WRF physics options.

Physics	Scheme	Reference
Microphysics	WSM5	Hong et al. (2004)
PBL	MYJ	Janjić (1994)
Shortwave radiation	Dudhia	Dudhia (1989)
Longwave radiation	RRTM	Mlawer et al. (1997)
Land surface scheme	Noah LSM	Chen & Dudhia (2001)
Surface layer scheme	Monin-Obukhov	Monin & Obukhov (1954)
Cumulus	None	None
Surface urban physics	UCM	Chen et al. (2011)
Surface lake physics	LAKE	Gu et al. (2015)

Table 2. Lake and urban areas in six WRF simulations.

Scenario	Lake Area (km^2)	Urban Area (km^2)
CTRL	281	0
URB	0	1417
BASE	0	0
ULS	281	120
ULM	281	410
ULL	281	1136

Table 3. Statistics of the CTRL simulation results for 2-m temperature, 2-m relative humidity, hourly rain rate, and 10-m wind speed.

	Mean Bias	RMSE	Correlation	HR
T2 (°C)	-0.84	1.82	0.73	0.96
RH2 (%)	-2.08	6.48	0.70	0.81
Rain rate (mm)	0.06	4.67	0.58	0.92
UV10 ($m\ s^{-1}$)	1.76	2.99	0.78	0.62

Note. The statistics are averaged between 16 UTC18 July and 00 UTC 22 July over the 30 in-situ weather stations and corresponding model grids. The thresholds used for calculating the hit rate (HR) are 2 °C for T2, 2 % for RH2, 2 mm for Rain rate, and 2 $m\ s^{-1}$ for UV10.

List of Figures

Figure 1. (a) Three nested domains used for the numerical simulations with elevation shaded in color. (b) spatial extent of domain 3 (with elevation shaded in color). The red polygon represents the urban boundary (for the ULL scenario), and the green polygon represents the Baiyang Lake. Black circles in (b) denote surface weather stations and the star represents the radiosonde station. The dashed black box outlines the projection of maximum development for XNA.

Figure 2. Land use/land cover for six different numerical experiments. (a) CTRL, (b) URB, (c) BASE, (d) ULS, (e) ULM, and (f) ULL. The dashed box outlines the projection of maximum development for XNA.

Figure 3. Geopotential height (with contour at every 10 gpm) at 500 hPa, wind fields (vector, in m s^{-1}) at 500 hPa and IVT (shade, in kg m^{-1} s^{-1}) based on the FNL reanalysis fields for (a) 18 UTC 18 July, (b) 12 UTC 19 July, (c) 06 UTC 20 July and (d) 00 UTC 21 July 2016. The red rectangle outlines the innermost domain.

Figure 4. Time series of simulated and observed (a) 2-m temperature (T2, ℃), (b) 2-m relative humidity (RH2, %), (c) 10-m wind speed (UV10, m s^{-1}), and (d) rain rate (mm h^{-1}). Blue (red) lines indicate the median values of all the weather stations (corresponding model grids in the CTRL simulation). Shades represent the inter-quartile ranges.

Figure 5. Hourly rain rates (mm h^{-1}) at (a) (d) 22 UTC 19 July, (b) (e) 00 UTC 20 July, and (c) (f) 02 UTC 20 July 2016 from the CMORPH rainfall product (upper panel), and the CTRL simulation (lower panel). The CTRL simulation shows results from domain 3. Scatters represent gauge-based observations.

Figure 6. Vertical profiles of (a, d) temperature (in ℃), (b, e) water vapor mixing ratio (in g kg^{-1}), and wind speed (in m s^{-1}) at the radiosonde station and the corresponding model grid. (a-c) 12 UTC 19 July, (b-f) 00 UTC 20 July.

Figure 7. Time series of hourly rain rates averaged over XNA region (the black dashed box shown in Figure 1) for (a) BASE, CTRL and URB, (b) CTRL, ULS, ULM, and ULL. (c) shows differences in rainfall accumulation between CTRL, URB, ULS, ULM, ULL and BASE. The dashed lines in (a) and (b) indicate the dividing moment between the two storm episodes.

Figure 8. Differences of rainfall accumulation (in mm) for the first (upper panel) and second storm episode (lower panel) between (a, c) CTRL and BASE, (b, d) URB and BASE. Vectors represent wind fields of 500 hPa at 16 UTC 18 July and 17 UTC 19 July in CTRL and URB. The red polygon represents the extent of urban coverage. The green polygon represents the lake. The blue dashed lines highlight the location of cross sections used for the following analyses.

Figure 9. Differences of 2-m temperature (T2, shade, in K), 2-m specific humidity (Q2, contour at every 0.5 g kg^{-1}) and 10-m wind speed (UV10, shade, in m s^{-1}) (a, b, e, f) before the first storm episode (averaged during 17 UTC to 19 UTC 18 July) and (c, d, g, h) before the second storm episode (averaged during 12 UTC to 14 UTC 19 July) between CTRL, URB and BASE.

Figure 10. Cross sections of vertical velocity (shaded, m s^{-1}) and wind field profile (vectors, m s^{-1}) along line AB (shown in Figure 8) before the first storm episode (17 UTC 18 July, upper panel) and line CD before the second storm episode (14 UTC 19 July, lower panel) of BASE,

CTRL and URB. The blue horizontal solid lines represent the lake while the red horizontal solid lines represent the urban extent.

Figure 11. Time series of moisture budget components averaged over XNA (the black dashed box shown in Figure 1) for (a) CTRL, (b) URB, (c) BASE, (d) ULS, (e) ULM, and (f) ULL. Rain rate (mm h^{-1}), evaporation (mm h^{-1}), precipitable water (mm) and convergence of water vapor (mm h^{-1}) are represented by black, red, blue, and green curves, respectively. The dashed lines indicate the dividing moment between the two storm episodes.

Figure 12. Differences of rainfall accumulation (in mm) for the first (upper panel) and second storm episode (lower panel) between (a-g) three urban simulations and the CTRL simulation, (d, h) the ULL and URB simulation. Vectors represent wind fields of 500 hPa at 16 UTC 18 July and 17 UTC 19 July in ULS, ULM and ULL simulations. The red polygons represent the extent of urban coverage. The green polygons represent the Lake. The blue dashed lines highlight the location of cross sections used for the following analyses.

Figure 13. Differences of 2-m temperature (T2, shade, in K), 2-m specific humidity (Q2, contour at every 0.5 g kg^{-1}) and 10-m wind speed (UV10, shade, in m s^{-1}) (a-c, g-i) before the first storm episode (averaged during 17 UTC to 19 UTC 18 July) and (d-f, j-l) before the second storm episode (averaged during 12 UTC to 14 UTC 19 July) between ULS, ULM, ULL and CTRL.

Figure 14. Lifted Index before (a-f) the first storm episode and (g-l) the second storm episode for the six scenarios.

Figure 15. Cross sections of CAPE (shaded, J kg^{-1}) and CIN (contour at every 10 J kg^{-1}) along line AB at 20 UTC 18 July (left column) and line CD at 12 UTC 19 July (right column) of CTRL, ULS, ULM, and ULL. The solid black horizontal lines represent the urban area in the three simulations.

Figure 16. Cross sections of vertical velocity (shaded, in m s^{-1}) and mixing ratio (contour at every 2 g kg^{-1}) along line AB averaged from 20 UTC to 23 UTC 18 July (left column) and line CD averaged from 14 UTC to 17 UTC 19 July (right column). The solid black horizontal lines represent the urban area in the four simulations.

Figure 1.

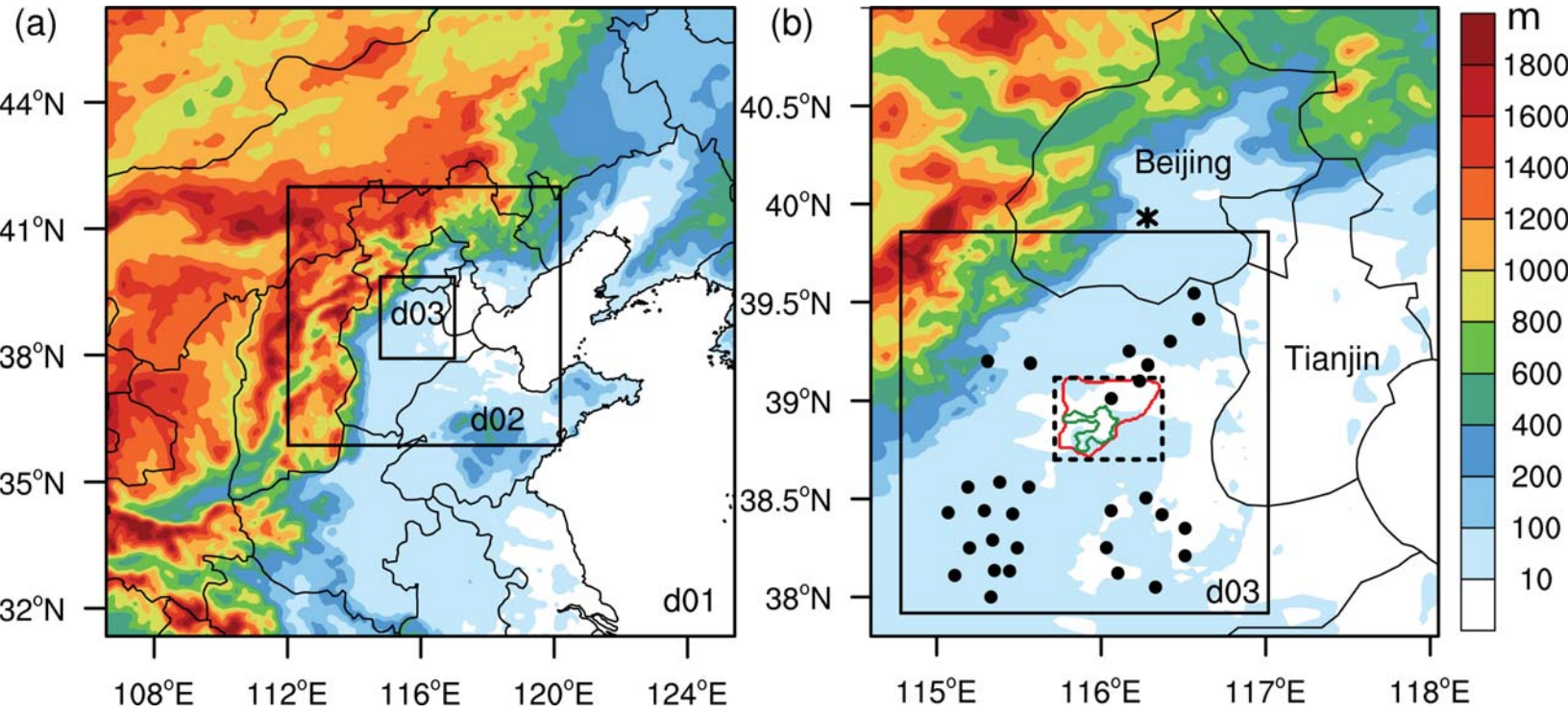
(a)
44°N
41°N
38°N
35°N
32°N
108°E
112°E
116°E
120°E
124°E
d03
d02
d01
(b)
40.5°N
40°N
39.5°N
39°N
38.5°N
38°N
115°E
116°E
117°E
118°E
Beijing
Tianjin
d03
m
1800
1600
1400
1200
1000
800
600
400
200
100
10

Figure 2.

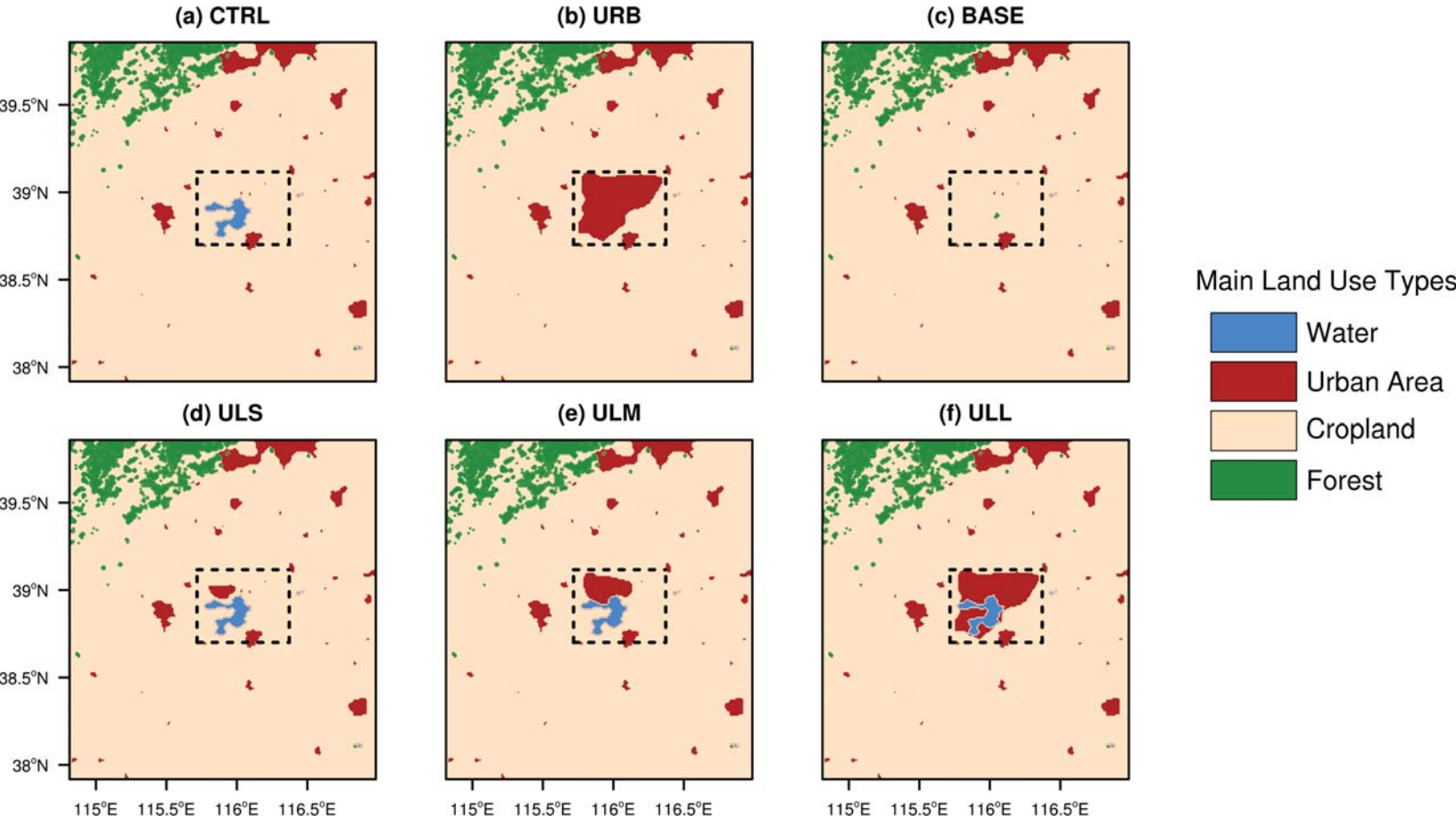
(a) CTRL
(b) URB
(c) BASE
(d) ULS
(e) ULM
(f) ULL
39.5°N
39°N
38.5°N
38°N
115°E
115.5°E
116°E
116.5°E
Main Land Use Types
Water
Urban Area
Cropland
Forest

Figure 3.

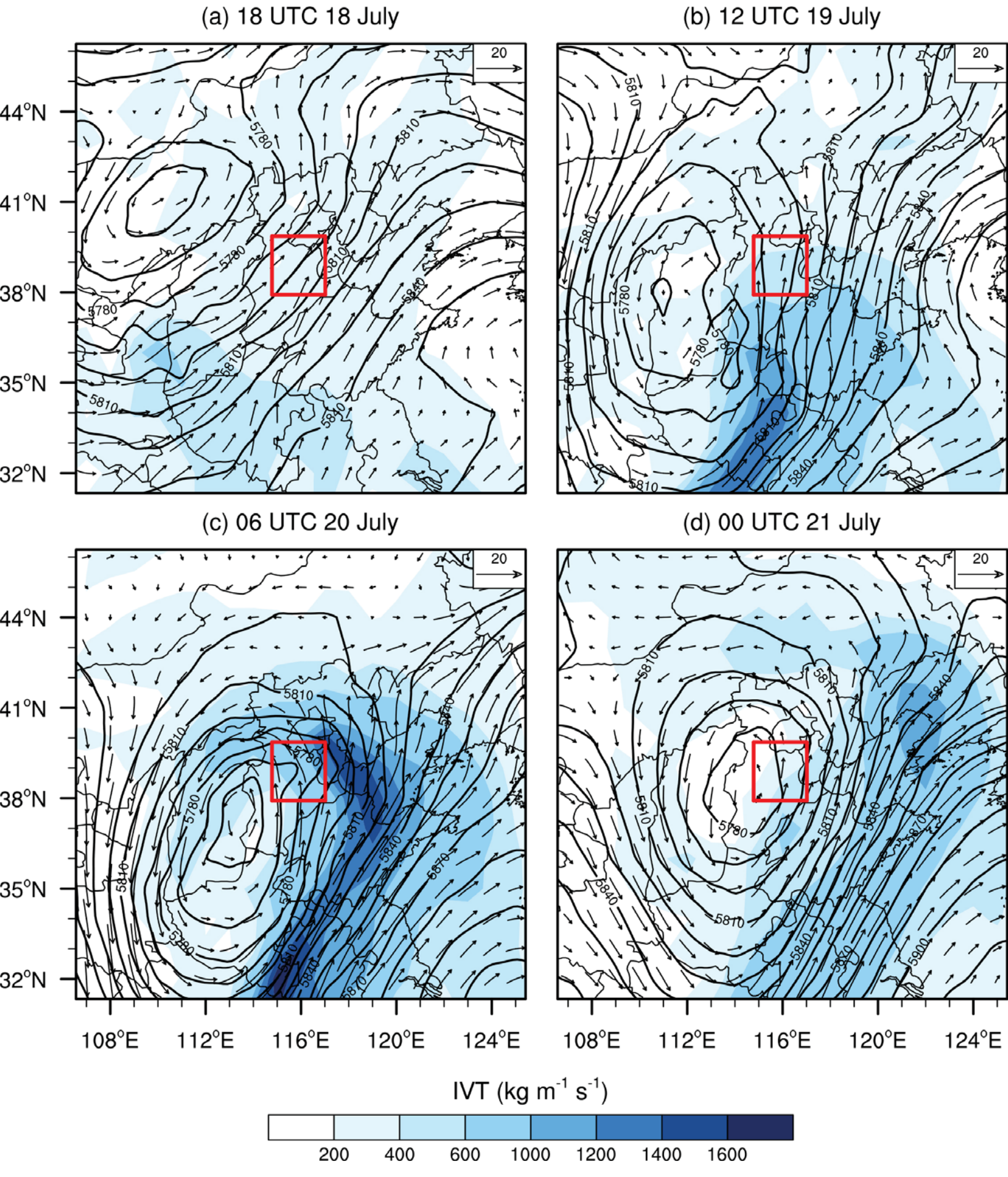
(a) 18 UTC 18 July
(b) 12 UTC 19 July
(c) 06 UTC 20 July
(d) 00 UTC 21 July
20
44°N
41°N
38°N
35°N
32°N
108°E
112°E
116°E
120°E
124°E
5780
5810
5840
5870
5900
IVT (kg m-1 s-1)
200
400
600
1000
1200
1400
1600

Figure 4.

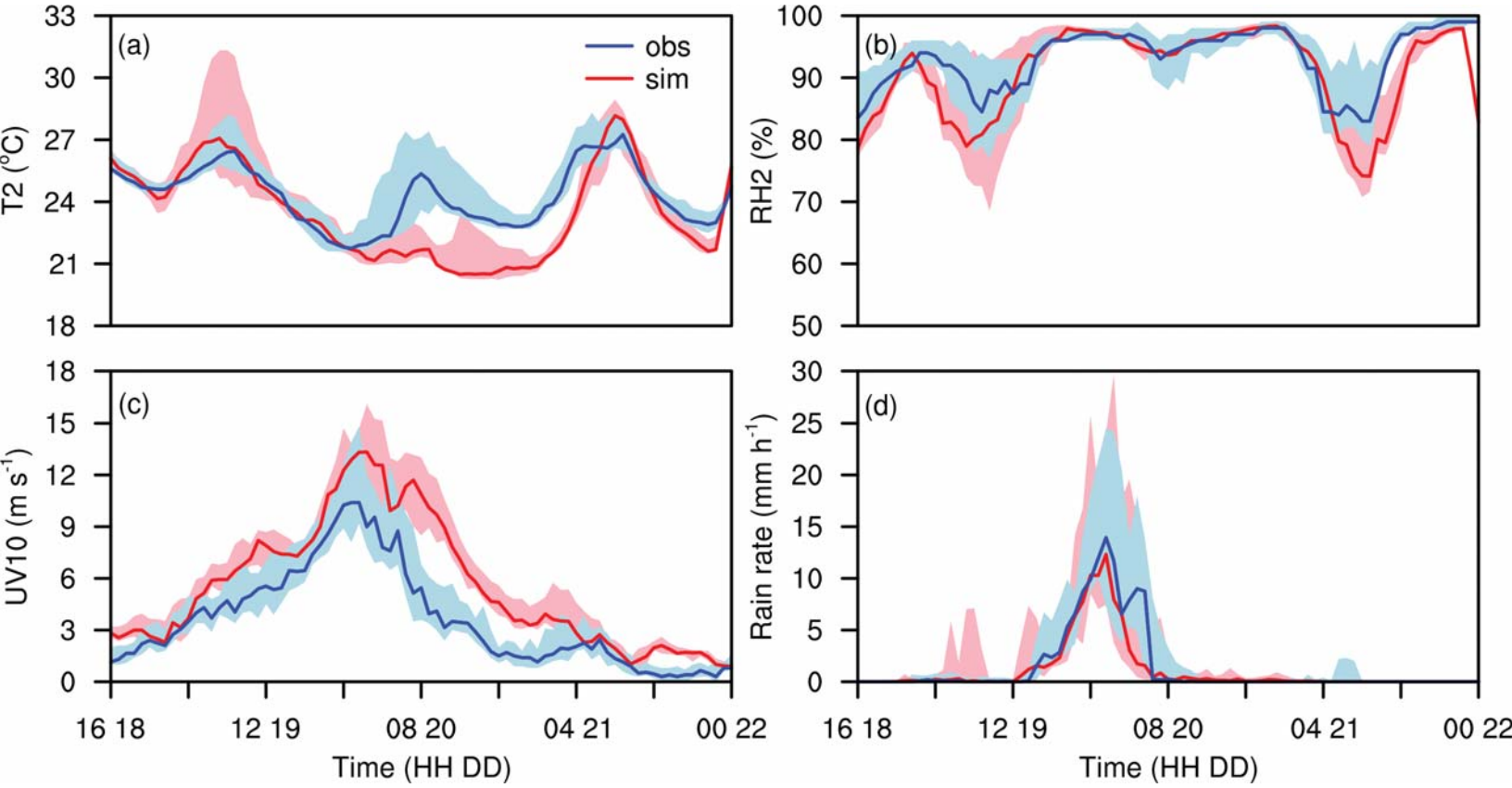
(a)
obs
sim
T2 (°C)
33
30
27
24
21
18
(b)
RH2 (%)
100
90
80
70
60
50
(c)
UV10 (m s-1)
18
15
12
9
6
3
0
(d)
Rain rate (mm h-1)
30
25
20
15
10
5
0
16 18
12 19
08 20
04 21
00 22
Time (HH DD)

Figure 5.

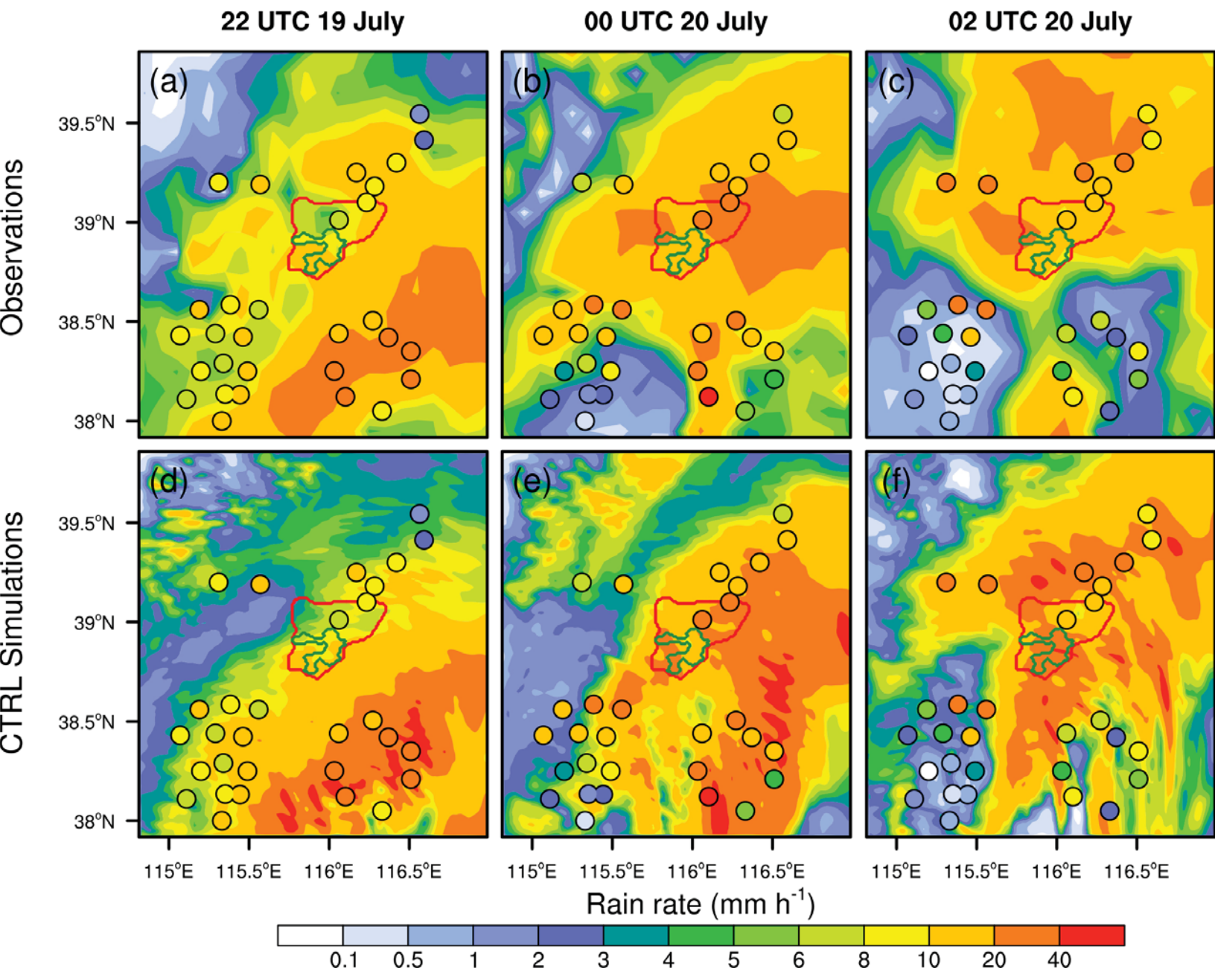
22 UTC 19 July
00 UTC 20 July
02 UTC 20 July
Observations
CTRL Simulations
(a)
(b)
(c)
(d)
(e)
(f)
39.5°N
39°N
38.5°N
38°N
115°E
115.5°E
116°E
116.5°E
Rain rate (mm h-1)
0.1
0.5
1
2
3
4
5
6
8
10
20
40

Figure 6.

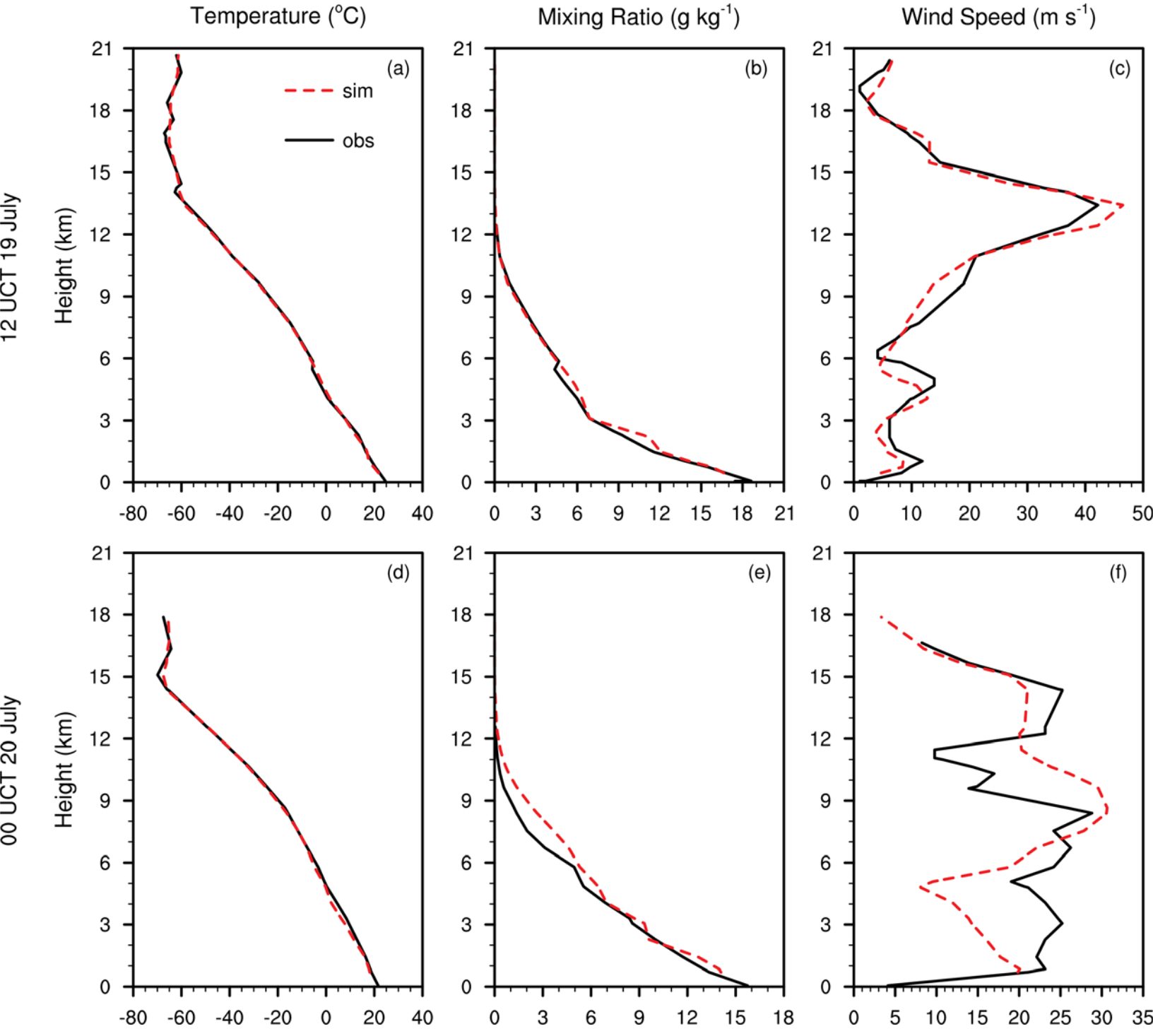
Temperature (°C)
Mixing Ratio (g kg-1)
Wind Speed (m s-1)
12 UCT 19 July
00 UCT 20 July
Height (km)
(a)
(b)
(c)
(d)
(e)
(f)
sim
obs
-80 -60 -40 -20 0 20 40
0 3 6 9 12 15 18 21
0 10 20 30 40 50
0 5 10 15 20 25 30 35

Figure 7.

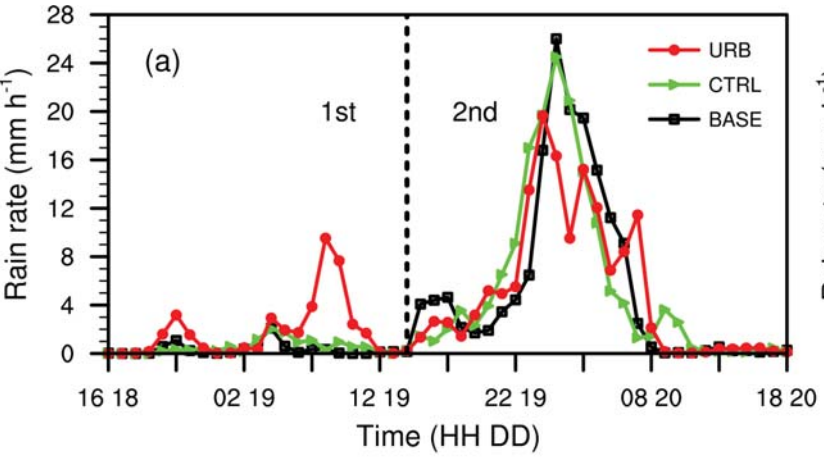
(a)
1st
2nd
URB
CTRL
BASE
Rain rate (mm h-1)
Time (HH DD)
16 18
02 19
12 19
22 19
08 20
18 20

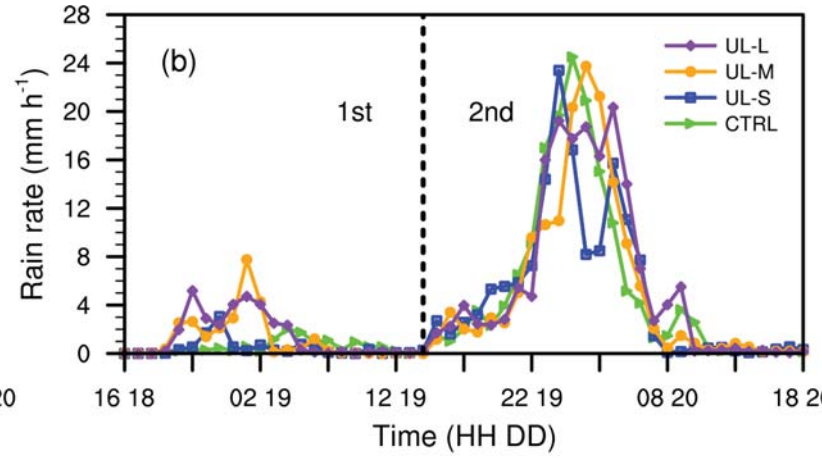
(b)
1st
2nd
UL-L
UL-M
UL-S
CTRL
Rain rate (mm h-1)
Time (HH DD)
16 18
02 19
12 19
22 19
08 20
18 20

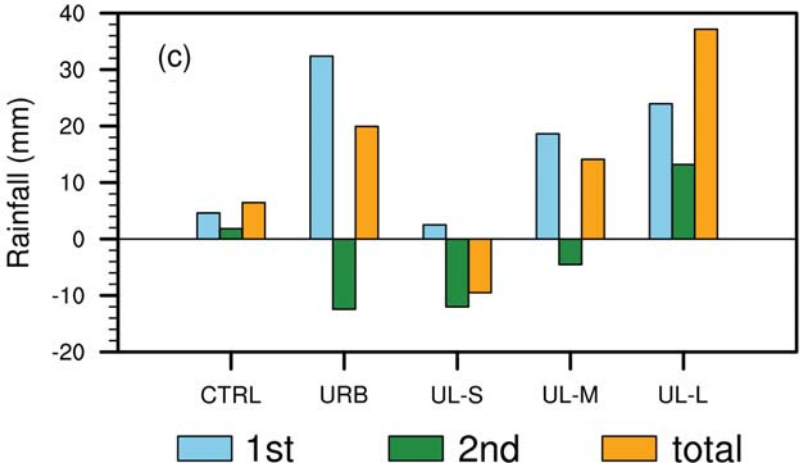
(c)
Rainfall (mm)
CTRL
URB
UL-S
UL-M
UL-L
1st
2nd
total

Figure 8.

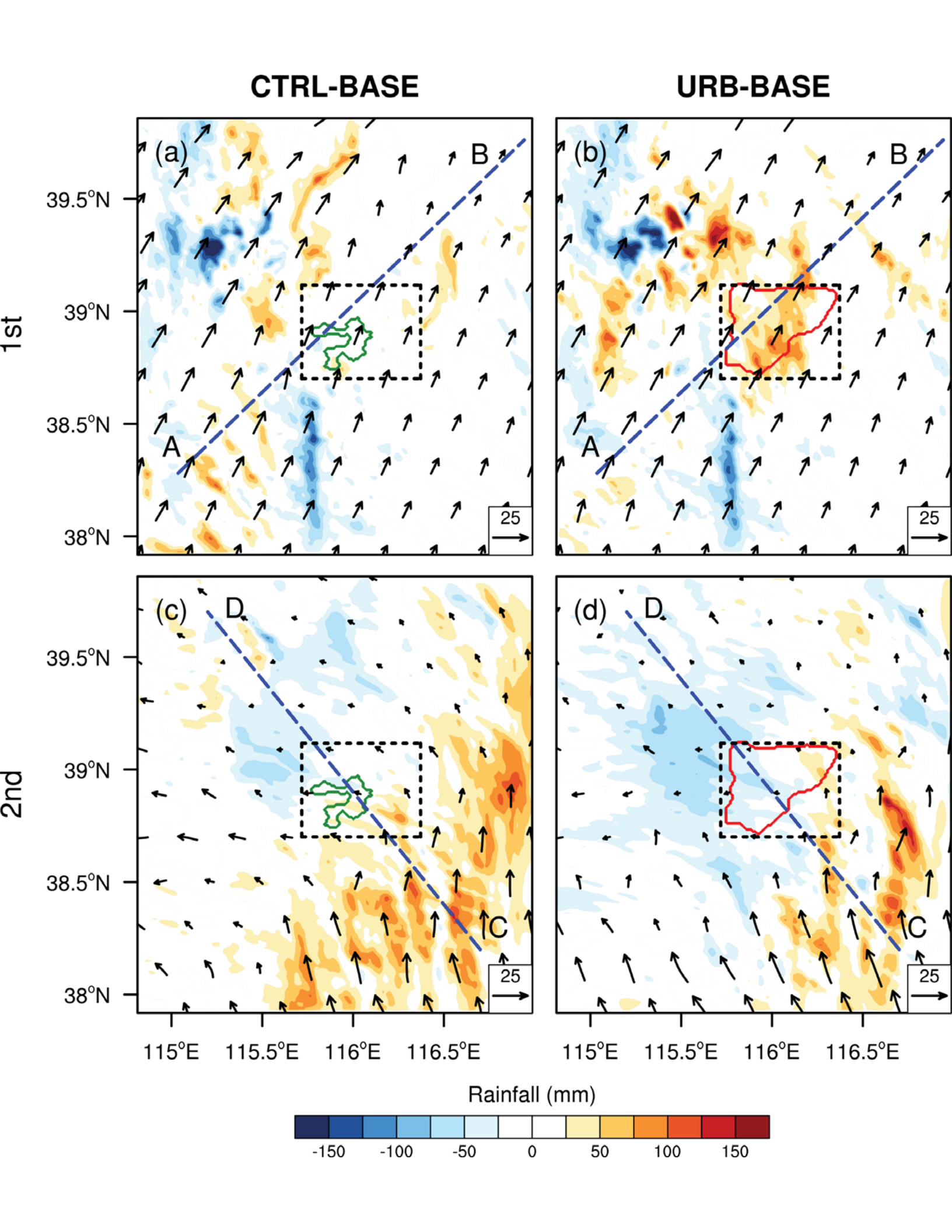
CTRL-BASE
URB-BASE
1st
2nd
(a)
(b)
(c)
(d)
A
B
C
D
39.5°N
39°N
38.5°N
38°N
115°E
115.5°E
116°E
116.5°E
25
Rainfall (mm)
-150
-100
-50
0
50
100
150

Figure 9.

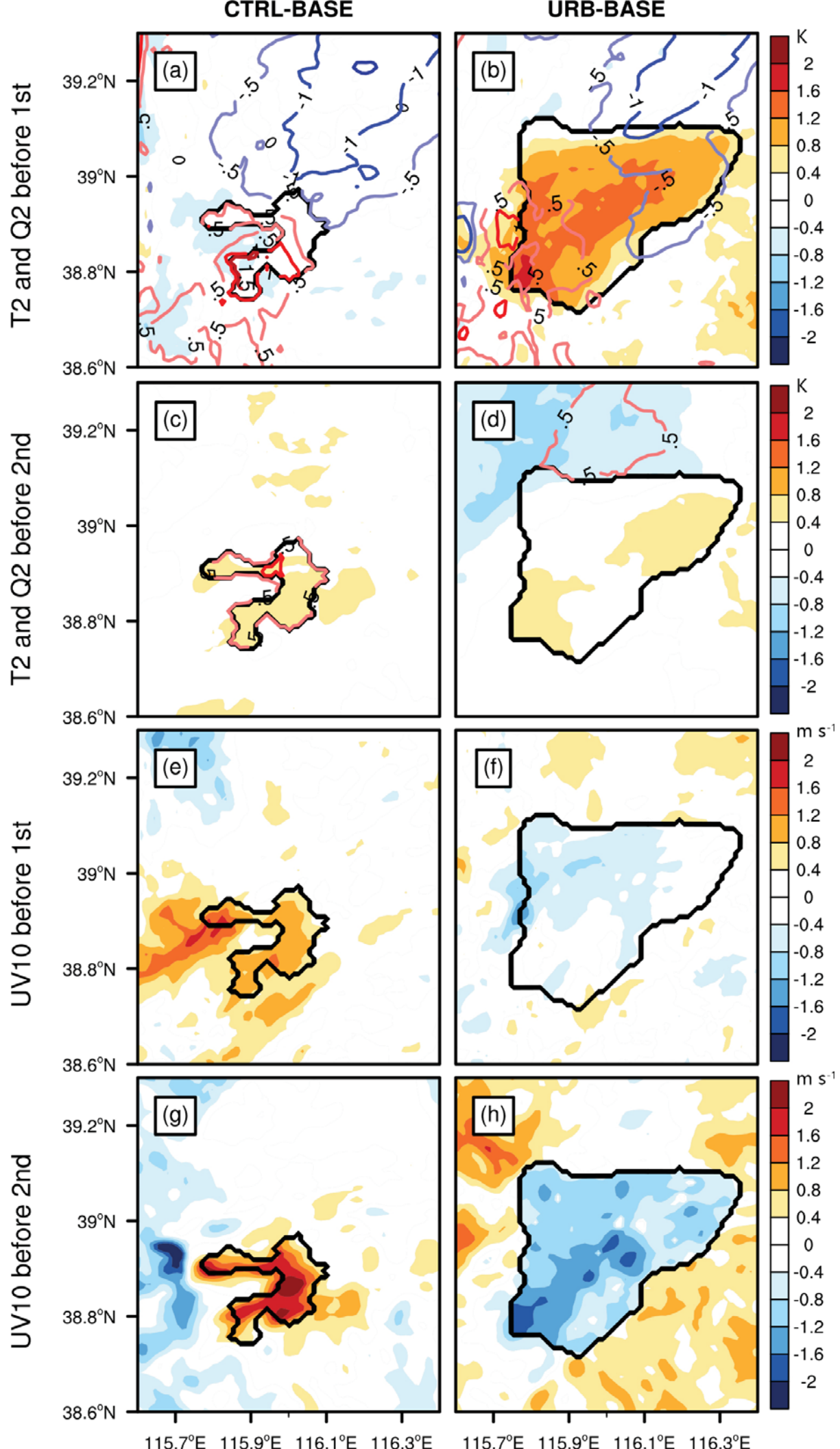
CTRL-BASE
URB-BASE
T2 and Q2 before 1st
T2 and Q2 before 2nd
UV10 before 1st
UV10 before 2nd
(a)
(b)
(c)
(d)
(e)
(f)
(g)
(h)
39.2°N
39°N
38.8°N
38.6°N
115.7°E
115.9°E
116.1°E
116.3°E
K
m s-1
2
1.6
1.2
0.8
0.4
0
-0.4
-0.8
-1.2
-1.6
-2

Figure 10.

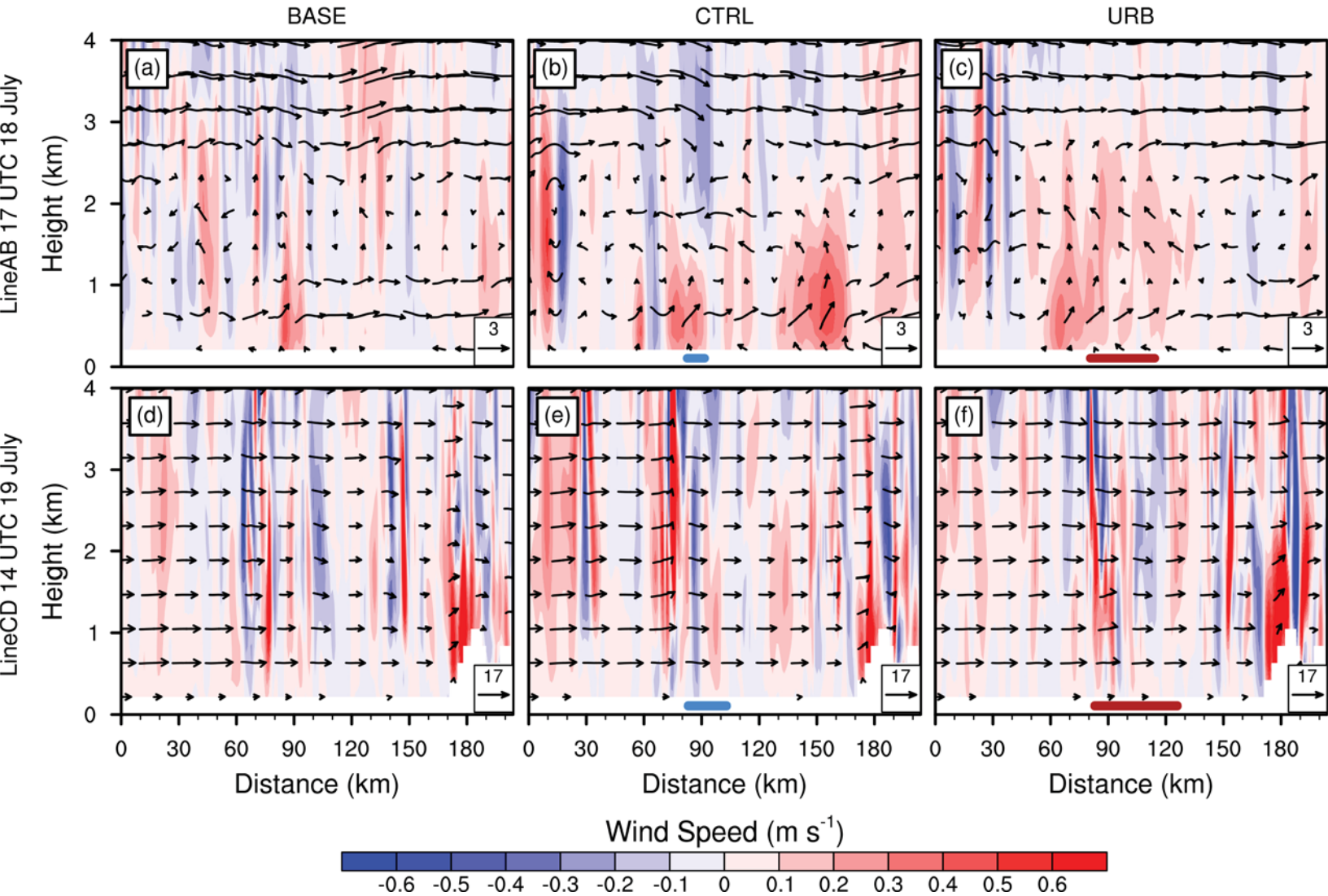
BASE
CTRL
URB
LineAB 17 UTC 18 July
LineCD 14 UTC 19 July
Height (km)
Distance (km)
(a)
(b)
(c)
(d)
(e)
(f)
3
17
0
30
60
90
120
150
180
1
2
3
4
Wind Speed (m s-1)
-0.6
-0.5
-0.4
-0.3
-0.2
-0.1
0
0.1
0.2
0.3
0.4
0.5
0.6

Figure 11.

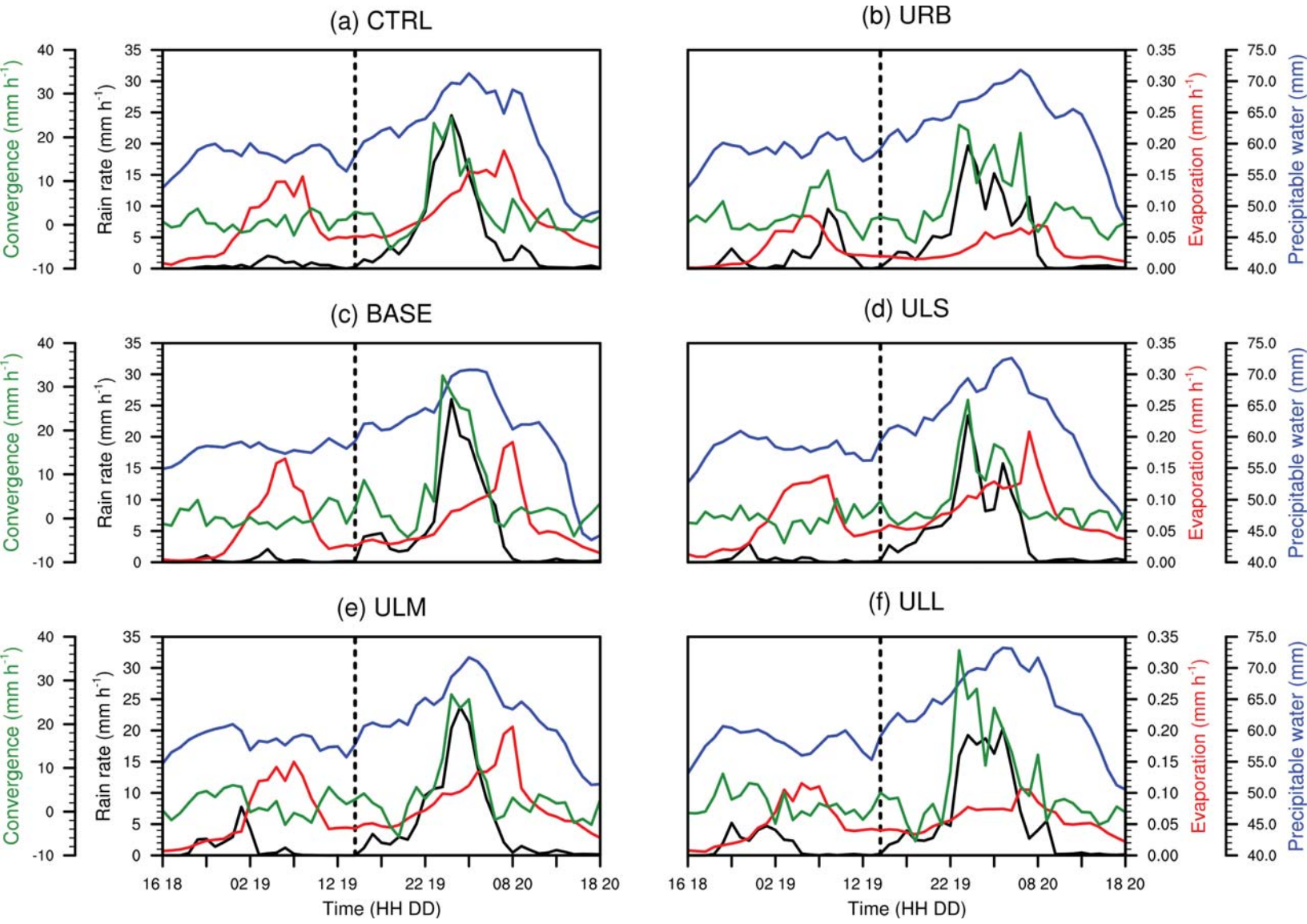
(a) CTRL
(b) URB
(c) BASE
(d) ULS
(e) ULM
(f) ULL
Convergence (mm h-1)
Rain rate (mm h-1)
Evaporation (mm h-1)
Precipitable water (mm)
16 18
02 19
12 19
22 19
08 20
18 20
Time (HH DD)

Figure 12.

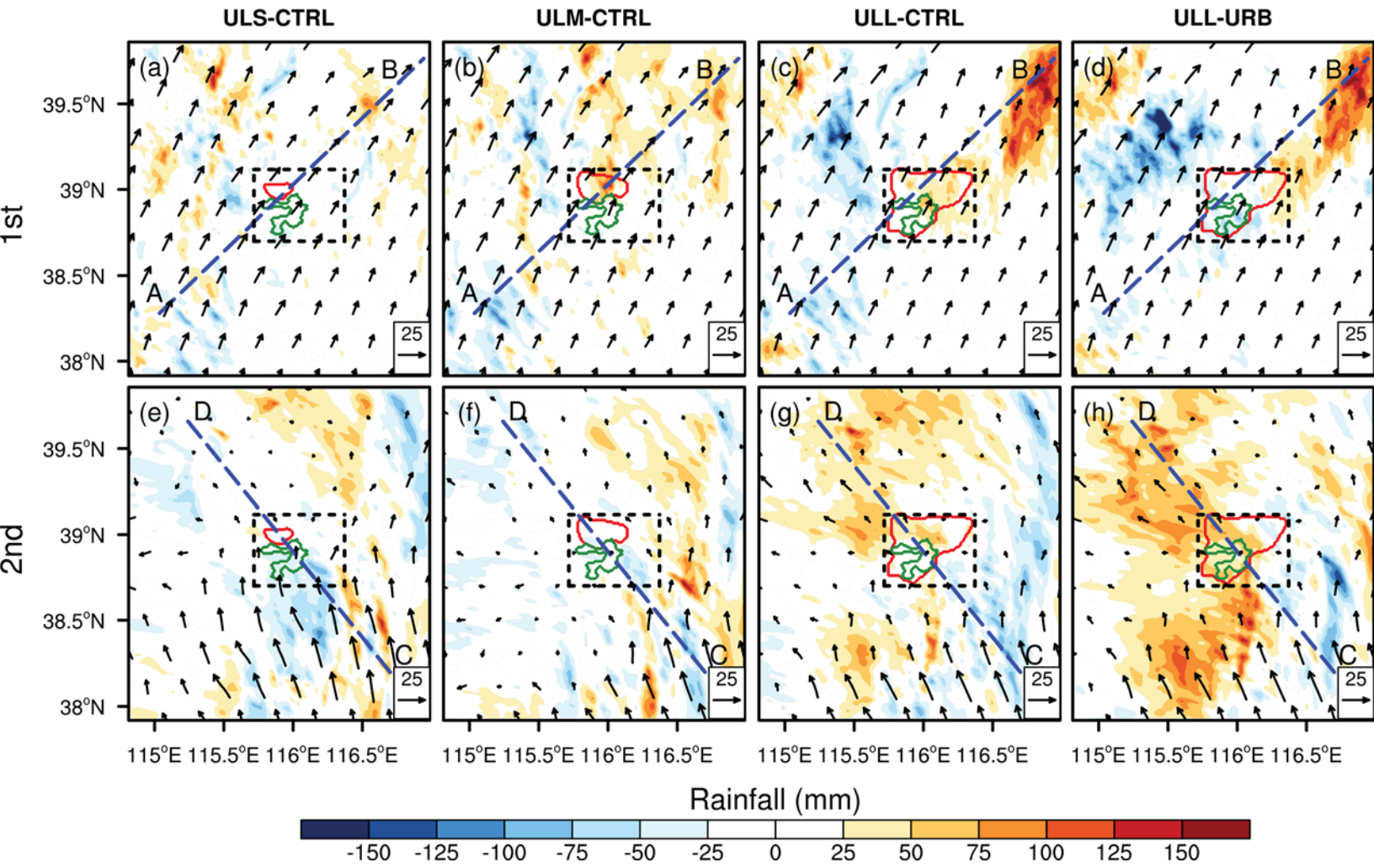
ULS-CTRL
ULM-CTRL
ULL-CTRL
ULL-URB
(a)
(b)
(c)
(d)
(e)
(f)
(g)
(h)
A
B
C
D
25
1st
2nd
39.5°N
39°N
38.5°N
38°N
115°E 115.5°E 116°E 116.5°E
Rainfall (mm)
-150 -125 -100 -75 -50 -25 0 25 50 75 100 125 150

Figure 13.

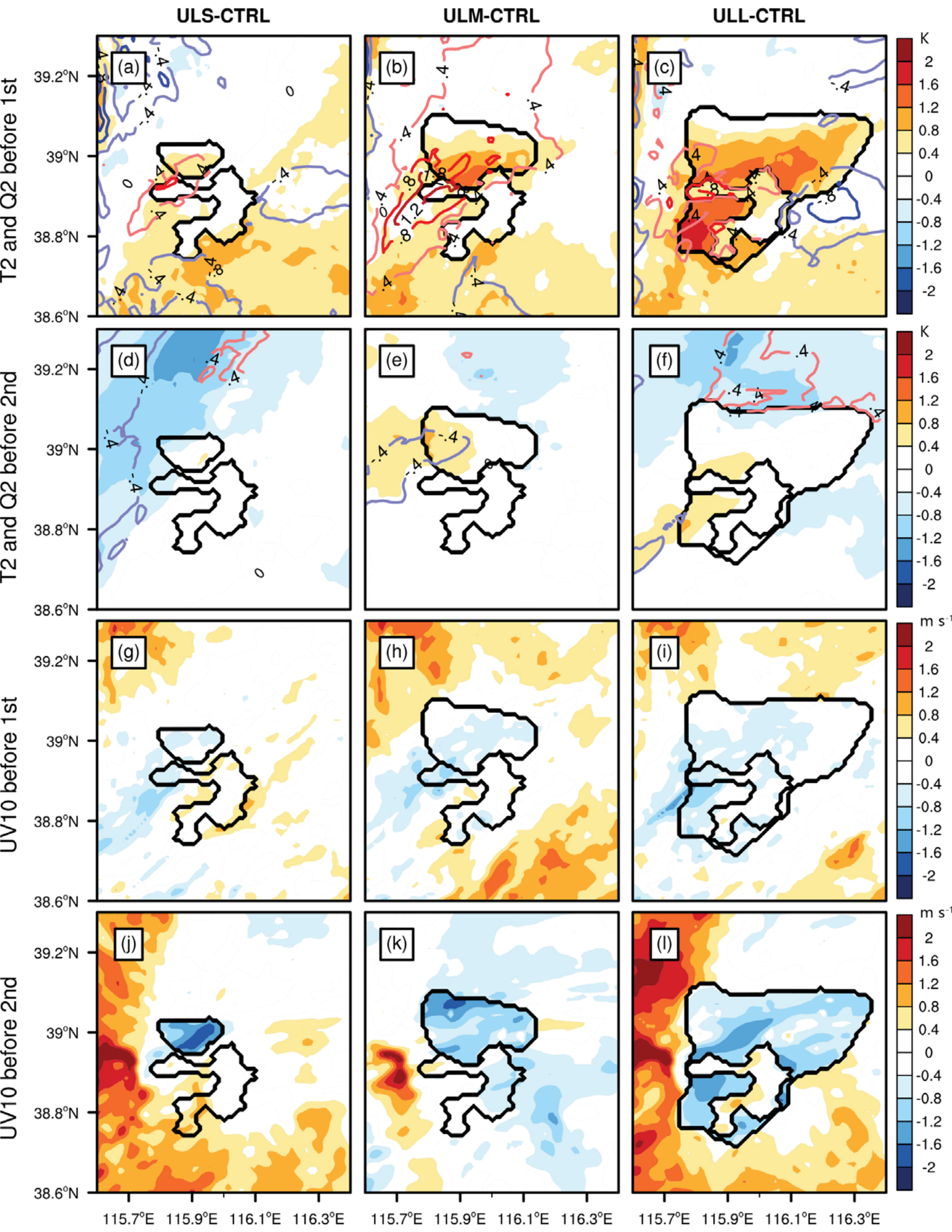
ULS-CTRL
ULM-CTRL
ULL-CTRL
T2 and Q2 before 1st
T2 and Q2 before 2nd
UV10 before 1st
UV10 before 2nd
(a)
(b)
(c)
(d)
(e)
(f)
(g)
(h)
(i)
(j)
(k)
(l)
39.2°N
39°N
38.8°N
38.6°N
115.7°E
115.9°E
116.1°E
116.3°E
K
m s-1
2
1.6
1.2
0.8
0.4
0
-0.4
-0.8
-1.2
-1.6
-2

Figure 14.

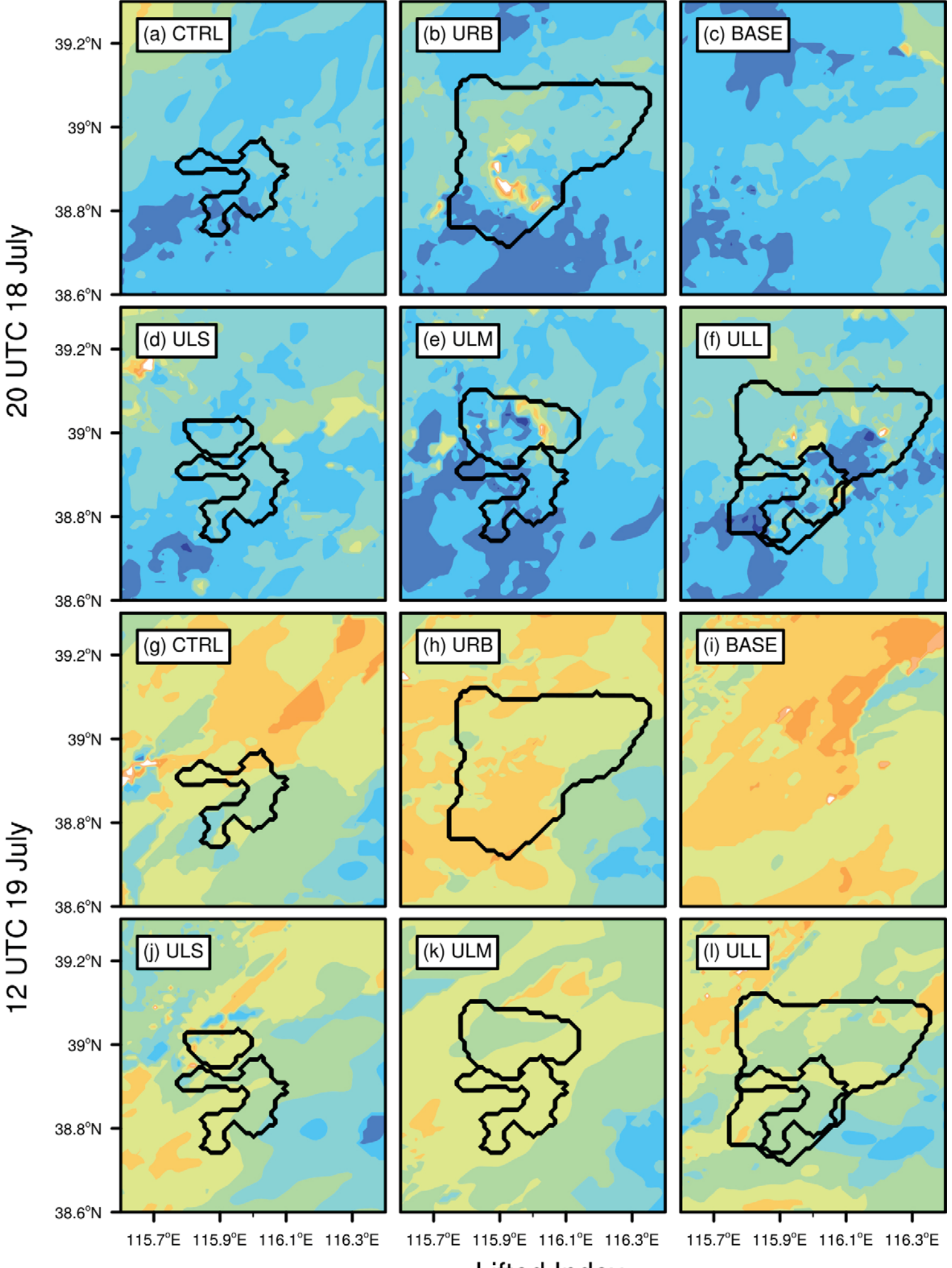
(a) CTRL
(b) URB
(c) BASE
(d) ULS
(e) ULM
(f) ULL
(g) CTRL
(h) URB
(i) BASE
(j) ULS
(k) ULM
(l) ULL
20 UTC 18 July
12 UTC 19 July
39.2°N
39°N
38.8°N
38.6°N
115.7°E
115.9°E
116.1°E
116.3°E
Lifted Index
-8
-7
-6
-5
-4
-3
-2
-1
0

Figure 15.

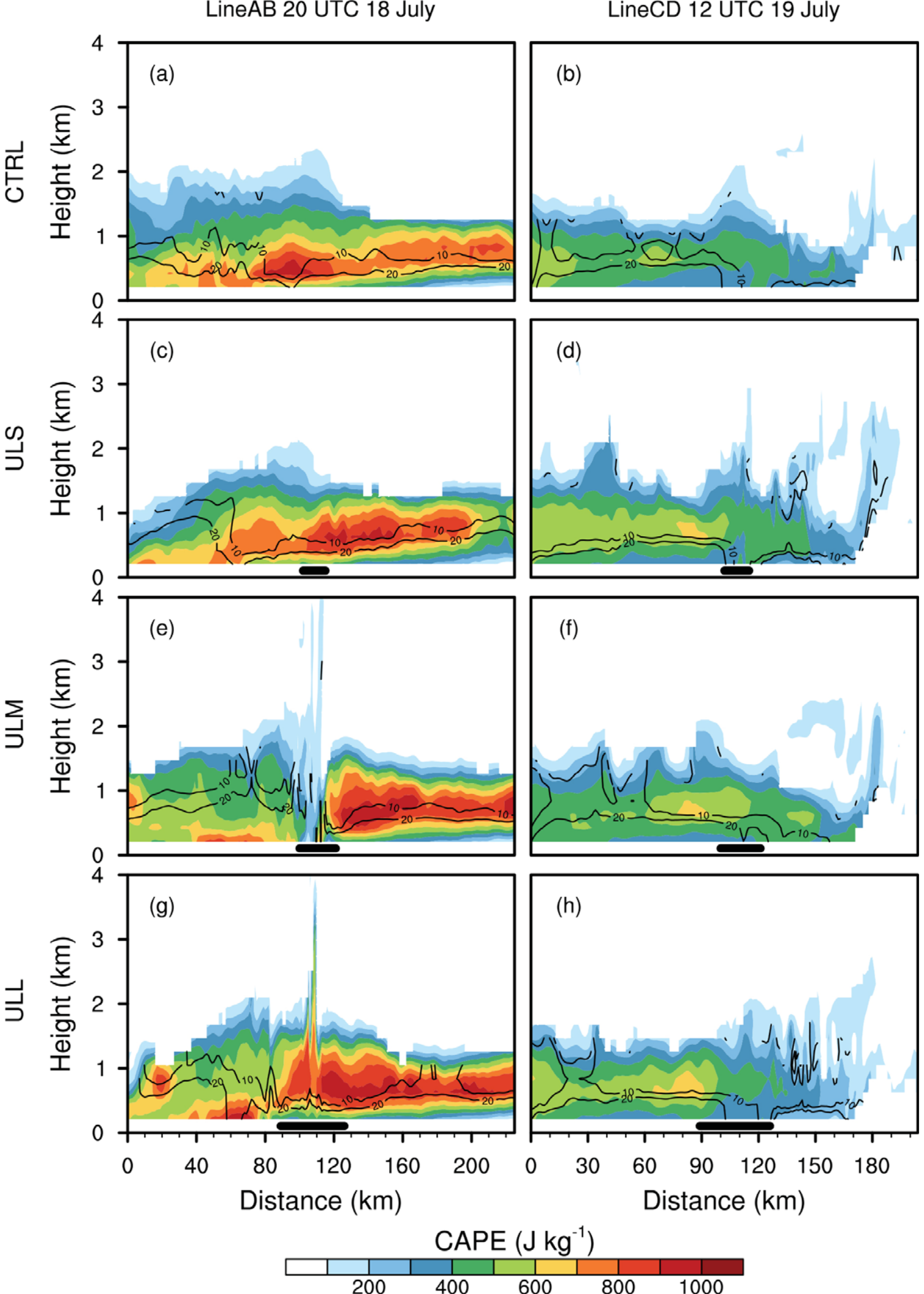
LineAB 20 UTC 18 July
LineCD 12 UTC 19 July
CTRL
ULS
ULM
ULL
(a)
(b)
(c)
(d)
(e)
(f)
(g)
(h)
Height (km)
Distance (km)
0
40
80
120
160
200
30
60
90
150
180
1
2
3
4
10
20
CAPE (J kg-1)
200
400
600
800
1000

Figure 16.

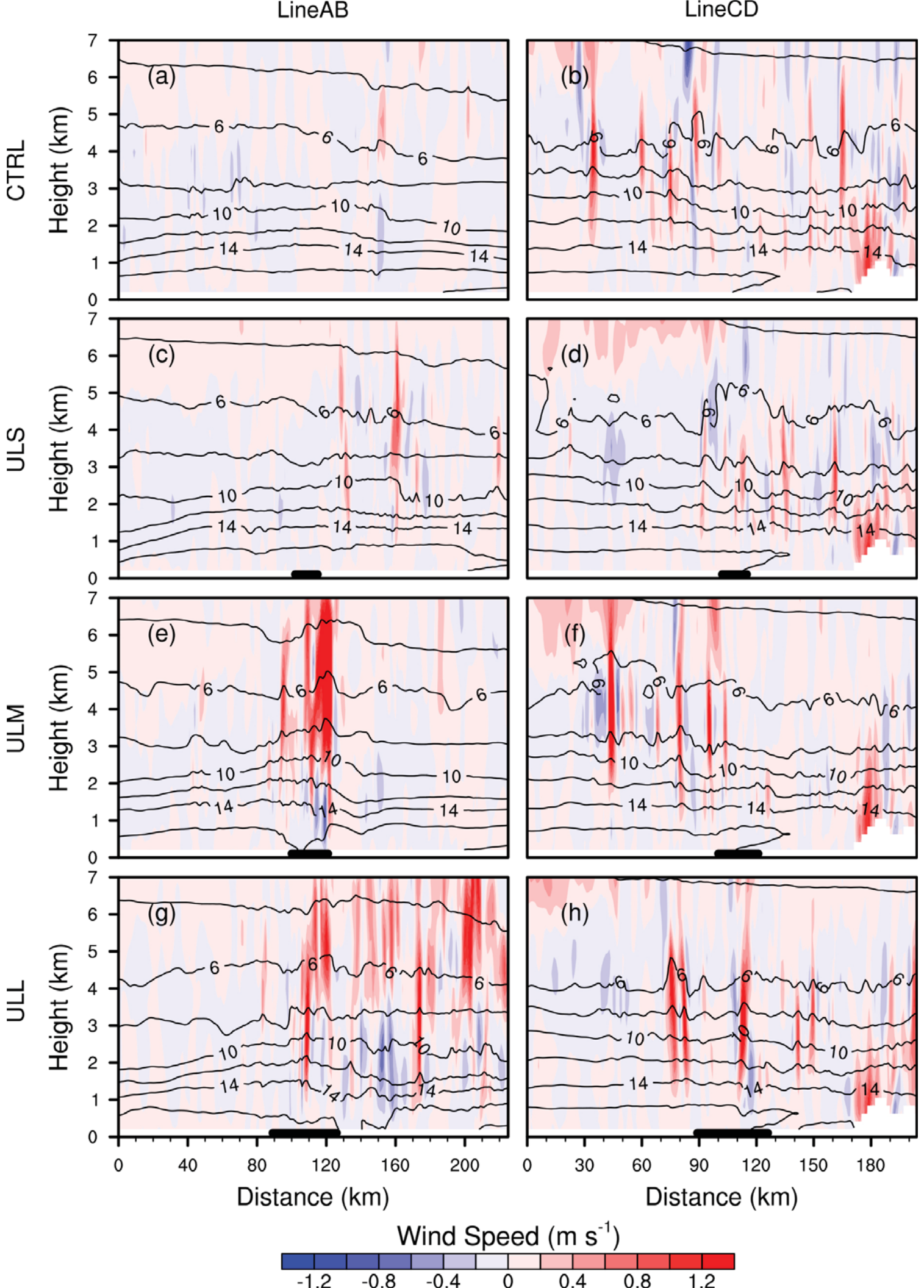
LineAB
LineCD
CTRL
ULS
ULM
ULL
Height (km)
(a)
(b)
(c)
(d)
(e)
(f)
(g)
(h)
Distance (km)
Distance (km)
Wind Speed (m s-1)
-1.2
-0.8
-0.4
0
0.4
0.8
1.2